The Influence of Magnetic Field Geometry on the Evolution of Black Hole Accretion Flows: Similar Disks, Drastically Different Jets

Kris Beckwith and John F. Hawley

Astronomy Department
University of Virginia
P.O. Box 400325
Charlottesville, VA 22904-4325

`krb3u@virginia.edu; jh8h@virginia.edu`

and

Julian H. Krolik

Department of Physics and Astronomy
Johns Hopkins University
Baltimore, MD 21218

`jhk@pha.jhu.edu`

ABSTRACT

Because the magnetorotational instability is capable of exponentially amplifying weak preexisting magnetic fields, it might be hoped that the character of the magnetic field in accretion disks would be independent of the nature of the seed field. However, the divergence-free nature of magnetic fields in highly conducting fluids ensures that their large-scale topology is preserved, no matter how greatly the field intensity is changed. By performing global two-dimensional and three-dimensional general relativistic magnetohydrodynamic disk simulations with several different topologies for the initial magnetic field, we explore the degree to which the character of the flows around black holes depends on the initial topology. We find that while the qualitative properties of the accretion flow are nearly independent of field topology, jet-launching is very sensitive to it: a sense of vertical field consistent for at least an inner disk inflow time is essential to the support of strong jets.

Subject headings: Black holes - magnetohydrodynamics - stars:accretion

1. Introduction

Magnetic fields are now generally acknowledged to be essential to accretion (Balbus & Hawley 1998). Amplified exponentially from weak seed fields by the magneto-rotational instability (MRI), they are stretched in a consistent direction so as to produce a net stress $\langle -B_r B_\phi \rangle / 4\pi$ capable of carrying enough angular momentum outward through the disk to support sizable accretion rates. Because the nonlinear state of the MRI is fully-developed magnetohydrodynamic (MHD) turbulence, it is often thought (or at least hoped) that its properties have little to do with the character of the seed magnetic field brought to the disk with the accretion flow.

However, there are certain properties of the magnetic field that are preserved despite the development of nonlinear turbulence. Because magnetic fields are divergence-free and the plasma in accretion flows has very little electrical resistivity, the global topology of the field persists, no matter what happens. It is therefore natural to ask whether any interesting properties of the accretion flow may depend on the global field topology. For example, could the field topology alter the relation between surface density and accretion rate? Or how the stress varies through the marginally stable region?

In addition to swallowing matter, accreting black holes often expel relativistic jets. Although the mechanisms by which these jets are launched have long been the subject of investigation and speculation, the current consensus focuses on a combination of large-scale magnetic fields and the rotation of either the central hole, the accretion disk, or both. Two specific MHD models have received the greatest attention: the Blandford-Znajek mechanism (Blandford & Znajek 1977) and the Blandford-Payne mechanism (Blandford & Payne 1982). In the Blandford-Payne model a large-scale vertical magnetic field is anchored in the disk, rotating with the orbital frequency. Above and below the disk magnetic tension dominates, and the field lines force the matter to rotate with this same frequency. If the fieldlines are angled outward sufficiently with respect to the disk, there can be a net outward force, accelerating the matter along the rotating fieldlines. The Blandford-Znajek model also depends upon rotating field lines, but the source of that rotation (and the source of the power in the jet) is the black hole rather than the disk: any field lines connecting the immediate vicinity of the black hole to infinity are forced to rotate by frame-dragging, so that Poynting flux carries off the energy.

Given the strong dependence of both the Blandford-Znajek and the Blandford-Payne mechanisms on the nature of the magnetic field in the disk and near the black hole, it is equally natural to inquire whether the topology of the field embedded in the accretion flow has any influence on their operation.

It is the goal of this paper to begin to investigate these questions, both as they relate to accretion disk dynamics and as they relate to jet properties. Unfortunately, it is difficult even to scratch the surface by purely analytic techniques (although there have been some attempts using highly-simplified models: Krolik 1999; Gammie 1999). On the other hand, direct numerical simulations provide a means by which aspects of these problems can be investigated in detail. Hawley & Krolik (2002) made a first exploration of the dependence of accretion properties on field topology in a highly-simplified approximation: Newtonian dynamics in a pseudo-Newtonian potential. They found that a purely toroidal initial field led to a systematically smaller accretion rate than one whose initial field was dipolar.

More recently, fully general relativistic MHD (GRMHD) simulations have become possible (McKinney & Gammie 2004; De Villiers et al. 2005; Hawley & Krolik 2006). These works have focused primarily on a single initial field structure: a set of nested dipole field loops contained entirely within the initial gas torus. Other field geometries have been examined, but only in rather limited fashion. For example, De Villiers et al. (2005) simulated the evolution of a torus with an initial toroidal field around a Schwarzschild black hole and noted the lack of any resulting jet, but did not consider why no jet formed. McKinney & Gammie (2004), using axisymmetric simulations, compared the electromagnetic luminosity of the standard dipole jet with that resulting from a few alternate magnetic field topologies. In particular, they studied cases in which the initial field was arranged in loops of alternating sign arranged either vertically or horizontally within the initial torus. The principal effect they reported was a factor of 2–3 reduction in the ratio of the time-averaged jet Poynting flux to the mean mass accretion rate. They also noted that an initial field that is purely vertical led to significant enhancements in both the mean mass accretion rate and the time-averaged jet Poynting flux. Axisymmetric simulations of tori threaded by net vertical field led De Villiers (2006) to concur that such a field can greatly enhance jet power. On the basis of these results, McKinney & Narayan (2007a) proposed that black holes inevitably become threaded by an organized vertical field if the initial disk contains a large-scale poloidal field with few parity changes. The intriguing character of these results motivates a more systematic study, one that employs three-dimensional simulations, considers the accretion flow as well as the jet, and investigates time-dependence.

The question immediately arises: how can one best attempt to describe the very complex mixture of topologies likely to be found in real accretion flows? The magnetic field near a black hole can be thought of as simply what the accretion process itself has self-consistently brought there from whatever source supplies it. In order to gain understanding of what, in realistic circumstances, must be a truly complex combination of structures, in this paper we do not try to construct a single "realistic" field geometry; instead, we study the effects due to individual members of a "basis set" of field topologies. Our hope is that by understanding

the action of pure types, we can gain some understanding of how realistic mixtures behave.

To be specific, we will begin with a carefully chosen set of different kinds of closed field loops that we expect to be generic. Closed field loops have the advantage of requiring many fewer free parameters to describe them fully within a simulation than do field geometries with net flux. Net flux geometries may well exist in Nature and have important effects; we will consider them in the second stage of this project. We begin with the conjecture that, at a qualitative level, the different sorts of closed field loop behavior can all be represented by a combination of those due to: dipolar loops, or fieldlines initially entirely poloidal and which cross the equatorial plane at well-separated radii; toroidal loops, which encircle the black hole; and quadrupolar loops, which (again, in the initial state) are poloidal, but close without crossing the equatorial plane. For each of these cases, we have run a lengthy three-dimensional GRMHD simulation whose results we hope characterize the accretion flow structure created by that field topology.

We have also run a series of high resolution axisymmetric simulations of each of the initially poloidal topologies (i.e. dipole and quadrupole). In addition, in order to understand better the implications of the finite lifetimes of closed loops, we have performed an axisymmetric simulation whose initial magnetic field structure was a series of dipolar loops, each contained within a span of radii narrow enough that the difference in inflow times across a loop is comparable to the equilibration time for the magnetic field in the jet.

The rest of this work is structured as follows. In §2 we briefly review the numerical scheme employed to solve the equations of GRMHD and give a detailed description of the initial conditions used to generate each topology. In §3 we examine the late time accretion flow structure that evolves from each of the initial field topologies, paying attention to each of the structures (main disk body, magnetized corona) that were identified by De Villiers et al. (2003) as arising from the evolution of the dipole field topology. In §4 we examine the properties of the third structure identified by De Villiers et al. (2003), the unbound outflow, and examine how the initial evolution of the field during the linear growth phase of the MRI gives rise to the components of the accretion flow at late times. Finally in §5 we summarize our results and highlight their importance for jets in astrophysical settings.

2. Numerical Details

In this work we undertake a study of both two- and three-dimensional simulations to investigate the influence of magnetic field topology on both the evolved accretion flow structure and relativistic jet formation. In doing so we continue a program of black hole accretion

disk simulations begun in De Villiers et al. (2003), Hirose et al. (2004), De Villiers et al. (2005), Krolik et al. (2005) and Hawley & Krolik (2006). Three-dimensional simulations, such as those presented in the previous work, are the only means by which one can gain insight into the evolved accretion flow properties due to the fundamental restriction posed by the anti-dynamo theorem (Moffatt 1978). Further, toroidal field models cannot be studied in axisymmetry, since the toroidal MRI requires nonzero azimuthal wavevectors. On the other hand, because jet formation occurs promptly during the evolution of the flow (Hawley & Krolik 2006), restrictions due to the anti-dynamo theorem are less critical for jet studies. In this case the higher resolution afforded by the two-dimensional simulations is particularly valuable.

The simulation code we use is described in De Villiers & Hawley (2003a). This code solves the equations of ideal non-radiative MHD in the static Kerr metric of a rotating black hole using Boyer-Lindquist coordinates. Values are expressed in gravitational units ($G = M = c = 1$) with line element $ds^2 = g_{tt}dt^2 + 2g_{t\phi}dtd\phi + g_{rr}dr^2 + g_{\theta\theta}d\theta^2 + g_{\phi\phi}d\phi^2$ and signature $(-, +, +, +)$. Since we are focusing in this paper on the influence of the magnetic field topology, we fix the black hole spin to $a/M = 0.9$ for all of the new simulations reported here.

The relativistic fluid at each grid zone is described by its density ρ, specific internal energy ϵ, 4-velocity U^μ, and isotropic pressure P. The relativistic enthalpy is $h = 1+\epsilon+P/\rho$. The pressure is related to ρ and ϵ via the equation of state for an ideal gas, $P = \rho\epsilon(\Gamma - 1)$. The magnetic field is described by two sets of variables. The first is the constrained transport magnetic field $\mathcal{B}^i = [ijk]F_{jk}$, where $[ijk]$ is the completely anti-symmetric symbol, and F_{jk} are the spatial components of the electromagnetic field strength tensor. From the constrained transport (CT) magnetic field components, we derive the magnetic field four-vector, $(4\pi)^{1/2}b^\mu = *F^{\mu\nu}U_\nu$, and the magnetic field scalar, $||b^2|| = b^\mu b_\mu$. The electromagnetic component of the stress-energy tensor is $T^{\mu\nu}_{(\mathrm{EM})} = \frac{1}{2}g^{\mu\nu}||b||^2 + U^\mu U^\nu||b||^2 - b^\mu b^\nu$.

In all of the simulations, the initial condition for the matter is an isolated, hydrostatic torus orbiting near the black hole. The initial state of the three-dimensional simulations was chosen so as to be consistent with that used in earlier simulations in this series (see De Villiers et al. 2003). The matter's adiabatic index, Γ was $5/3$ and the angular momentum distribution was slightly sub-Keplerian, with a specific angular momentum at the inner edge of the torus (located at $r = 15M$) $\ell_\mathrm{in} = 4.567$ (we define $\ell \equiv U_\phi/U_t$). For this choice of ℓ_in, the pressure maximum is at $r \approx 25M$.

In the two-dimensional simulations, our fiducial torus was chosen to have a constant angular momentum distribution with $\ell = 5.2$, Γ was $4/3$, and the inner edge was again located at $r = 15M$. This torus is significantly thicker than the nearly-Keplerian torus used

for the three-dimensional simulations; its density scale height at the pressure maximum, measured along surfaces of constant radius, is a factor ~ 1.3 greater than that of the three-dimensional torus. This thicker configuration makes it easier to resolve the multiple field loop model, where several field loops must fit into a restricted space. This specific combination of ℓ and Γ was also necessary to manipulate the shape of the torus so that there was an appropriate balance in magnetic flux between the different components of the multiple dipole loop simulation. In the quadrupolar field case, in order to study how the evolution of the field depends on its detailed geometry, we examined what happened as ℓ varied from 4.9 to 5.2 in steps of 0.05.

The initial torus is overlaid with a variety of magnetic field configurations, all with zero net flux. The initial poloidal magnetic field is determined from the curl of the four-vector potential, i.e., $F_{\mu\nu} = \partial_\mu A_\nu - \partial_\nu A_\mu$ with only $A_\phi \neq 0$. For a single dipolar loop, we set

$$A_\phi = A_0 \left(\rho - \rho_{cut} \right). \tag{1}$$

For a quadrupole, the azimuthal component of the vector potential is

$$A_\phi = A_0 \left(\rho - \rho_{cut} \right) r \cos \theta. \tag{2}$$

In both of these cases A_ϕ is set to zero where the density is less than ρ_{cut}; this device confines the initial field to lie well inside the torus. In all the poloidal simulations, the initial field intensity (i.e., the parameter A_0) is determined by setting the volume-averaged ratio of gas to magnetic pressure $\beta = 100$.

The vector potential for n dipolar loops (used only for the two-dimensional simulations) is more complicated. It is given by

$$A_\phi = A_0 \left(\rho - \rho_{cut} \right) \sum_{j=1}^{n} \frac{J_j R_j}{\sqrt{R_j^2 + r^2 + 2R_j r \sin \theta}} \left[\frac{\left(2 - k_j^2 \right) K(k_j) - 2E(k_j)}{k_j^2} \right], \tag{3}$$

where the total vector potential is the superposition of the (non-relativistic) vector potentials from n current loops (see Jackson 1975, Pg. 182, Eqn. 5.37). Here J_j is the current in the jth loop, located at radius R_j in the equatorial plane. K and E are the complete elliptic integrals of the first and second kinds, and $k_j = 4R_j r \sin \theta / (R_j^2 + r^2 + 2R_j r \sin \theta)$. The R_j are chosen so that the difference between the inflow times of adjacent loops is approximately equal to one jet equilibration time, ~ 700–$1000M$. The signs of the J_j alternate with increasing radius so that the senses of the dipolar field loops alternate. The magnitudes of the currents were chosen with the goal of ensuring that the evolution of the two radially innermost loops was governed by the field local to those loops. The purpose of this simulation was to study the interaction of the two inner loops as they accrete; in that context, the only function of the

two outer loops is to supply the outer part of the torus with magnetic field, so that it could accept the angular momentum brought to it from the true accretion flow. Thus, the most appropriate outer field structure for this particular numerical experiment is one that has the least influence on dynamics inside the pressure maximum. After some experimentation, we found that this goal could be achieved only by giving the two outer loops relatively small currents. When that was done, the outer two loops moved outward with the outer portion of the disk and were quickly destroyed (i.e. forced to reconnect) as the second loop from the inside expanded toward them. We make no pretense that this choice is a fair representation of generic four-loop evolution, but it does support our study of what happens when two complete loops of opposite sense are brought into the inner disk one after the other.

For a purely toroidal initial field, all that is necessary is to set $\mathcal{B}^r = \mathcal{B}^\theta = 0$ and determine $\mathcal{B}^\phi$ by a choice of volume-averaged β. Here we use $\beta = 10$, as, in the purely toroidal case, accretion can occur only once MRI-induced turbulence on the large scales has grown to sufficiently large amplitude, and long wavelength modes grow comparatively slowly. Beginning with a comparatively strong field ensured that accretion activity started soon after the simulation began. After saturation, the field (in relative terms) actually weakened somewhat: the volume-averaged β grew to ≈ 30 (see Section 3.1). As before, the initial magnetic field is set to zero for densities below ρ_{cut}.

We take the dipole simulation KDPg (originally presented in Hawley & Krolik 2006, where further discussion of our boundary conditions and grids may be found) as our fiducial three-dimensional run. The three-dimensional quadrupole simulation is designated QDPa and the three-dimensional toroidal simulation is TDPa. KDPg and QDPa were run for $10^4\ M$ in time, which corresponds to approximately 12 orbits at the initial pressure maximum. The toroidal field model, TDPa, evolves initially at a slower rate; it was run to $2.9 \times 10^4 M$ in time. For each simulation, the time step Δt was determined by the minimal light crossing time for a zone on the spatial grid and remained constant for the entire simulation (De Villiers & Hawley 2003a).

Each of the three-dimensional simulations used $192 \times 192 \times 64$ (r, θ, ϕ) grid zones. The radial grid extends from an inner boundary located at $r_{in} = 1.5M$, which lies just outside the black hole event horizon, to an outer boundary located at $r_{out} = 120M$. For the two poloidal topologies, the radial grid was graded using a hyperbolic cosine distribution; for the toroidal case a logarithmic distribution was used. An outflow condition is applied at both the inner and outer radial boundary. The θ-grid spans the range $0.045\pi \leq \theta \leq 0.955\pi$ using an exponential distribution that concentrates zones near the equator. A reflecting boundary condition is used along the conical cutout surrounding the coordinate axis. The ϕ-grid spans the quarter plane, $0 \leq \phi \leq \pi/2$, with periodic boundary conditions applied in ϕ. The use of

this restricted angular domain significantly reduces the computational requirements of the simulation.

The two-dimensional simulations were performed on a 1024×1024 (r, θ) grid in which the radial cells are graded logarithmically, and the polar angle cells are concentrated toward the equator in the same way as for the three-dimensional simulations. The θ grid, however, goes much closer to the axis than in the three-dimensional simulations, with a cut-out of only $10^{-5}\pi$ radians. In addition to allowing higher poloidal resolution at a reasonable computational cost, two-dimensional simulations have the additional advantage that field-lines can be easily visualized as level surfaces of the vector potential component A_ϕ. Using this approach, we illustrate the magnetic field topologies for the three different poloidal configurations in Figure 1.

3.   The Accretion Flow

We begin by examining the average properties of the accretion flows in simulations KDPg, QDPa and TDPa. De Villiers et al. (2003) described the accretion flow structure in terms of three distinct regions: the main disk body, the coronal envelope, and the unbound outflow. In this section, we study the first two, paying special attention to contrasts (or lack of contrast) when the magnetic topology changes. We will discuss the unbound outflow in the following section.

Much of the analysis will be in terms of various time- and space-averaged quantities. The radial profile of the time-averaged shell integral of $\mathcal{Q}$ is defined as

$$\langle \mathcal{Q}(r) \rangle_F = \frac{2}{\pi T} \int \sqrt{-g}\mathcal{Q}(t, r, \theta, \phi) dt d\theta d\phi \qquad (4)$$

Similarly, the shell average of a quantity $\mathcal{Q}$ at a radius r is defined to be:

$$\langle \mathcal{Q}(r) \rangle_S = \frac{\int \sqrt{-g}\mathcal{Q}(t, r, \theta, \phi) d\theta d\phi}{\int \sqrt{-g} d\theta d\phi} \qquad (5)$$

The angular profile of the time-average of $\mathcal{Q}$ at radius r is defined by

$$\langle \mathcal{Q}(\theta; r) \rangle_A = \frac{2}{\pi T} \int \sqrt{-g}\mathcal{Q}(t, r, \theta, \phi) dt d\phi. \qquad (6)$$

Lastly, the time- and volume-average of $\mathcal{Q}$ is:

$$\langle \mathcal{Q} \rangle_V = \frac{\int \sqrt{-g}\mathcal{Q}(t, r, \theta, \phi) dt dr d\theta d\phi}{\int \sqrt{-g} dt dr d\theta d\phi}. \qquad (7)$$

In these equations T is the time over which the integral is computed, and g is the usual metric determinant. Typically $T = 6000M$; for KDPg and QDPg this is the last $6000M$ of the full evolution, while for TDPa we choose a $6000M$ window in the middle of the simulation after the accretion flow is established. The spatial extent of the shell integration is the full θ and ϕ computational domain. During a given simulation, various shell integrals and radial fluxes are computed and stored every M in time. This data can then be integrated over time to obtain quantities such as the total or time-averaged jet outflow or accretion rate.

It is also useful to divide the shell and volume integrals into two parts, one for bound and one for unbound flow. For simplicity we define a particular zone to be "unbound" if $-hU_t > 1$. Unbound outflow can further be defined as those unbound cells with $U^r > 0$. In these simulations only the outflow near the axis (the jet outflow) is unbound; the coronal backflow from the disk itself remains bound.

3.1. Disk body

The initial evolution of the accretion disks in KDPg and QDPa is qualitatively similar. Both field configurations begin with considerable radial field within the torus. This is sheared out, generating toroidal field which, by $t \sim 500M$, is sufficiently strong that the resulting poloidal gradient in $||b||^2$ begins to drive the inner edge of the torus (initially located at $r = 15M$) inward. The inner edge of the disk arrives at the black hole at $t \sim 1000M$. Within the disk body, the MRI generates the turbulence that will determine the subsequent evolution of the disk, and by $t \sim 4000M$ a statistically stationary turbulent accretion flow has been established inside the radius of the inner edge of the initial torus.

The toroidal field model TDPa evolves more slowly than the two poloidal field cases, consistent with the results from earlier toroidal field pseudo-Newtonian simulations (Hawley & Krolik 2002). As discussed at length in Hawley & Krolik (2002), this behavior stems both from the absence of an initial radial field (which means that there is no toroidal field amplification due to shear) and from the fact that long-wavelength modes—which are the most effective in driving accretion—grow relatively slowly. Inflow can begin only when the MRI has produced turbulence of sufficient amplitude, which occurs by $t = 4000M$, corresponding to about 5 orbits at the radius of the torus pressure maximum. The accretion rate into the hole increases until about $t = 1.5 \times 10^4 M$, after which it shows large fluctuations without an overall trend.

Figure 2 shows time-averaged, shell-integrated radial profiles of a number of quantities relevant to the accretion flow: accretion rate $\dot{M} = \langle \rho U^r(r) \rangle_F$, surface density $\Sigma(r) = \langle \rho \rangle_F / \int \sqrt{g_{rr} g_{\phi\phi}} d\phi$, the net accreted angular momentum per unit rest mass, $L = \langle T^r_{\phi \, \text{(FL)}}(r) +$

$T^r_{\phi\,(\mathrm{EM})}(r)\rangle_F/\dot{M}$, $\langle||b||^2(r)\rangle_F$, the electromagnetic Poynting flux $\langle|T^r_t|_{(\mathrm{EM})}(r)\rangle_F$ and the EM angular momentum flux $\langle|T^r_\phi|_{(\mathrm{EM})}(r)\rangle_F$. The subscripts FL and EM denote the fluid and electromagnetic contributions to the stress-energy tensor, respectively. All quantities are computed in the coordinate frame after the turbulent accretion flow is established, and in all cases the volume integral was restricted to cells where the matter was bound. The poloidal field simulations were averaged over time $t = 4000–10000M$ while the toroidal field data were averaged over $t = 12500–18500M$.

These six plots may be divided into two groups: those with little dependence on initial field topology (surface density and accreted angular momentum per unit mass), and those with a stronger dependence (accretion rate, magnetic field strength, Poynting flux, and electromagnetic angular momentum flux). Although the radial distribution of the surface density in all three cases is fairly similar, there is a slight distinction between the two poloidal models on the one hand and the toroidal on the other. The surface density in the toroidal model rises somewhat more steeply with radius, with lower density near the black hole and higher values outside of $r/M = 7$. For all three topologies, the specific angular momentum carried into the hole is close to the angular momentum of the marginally stable orbit. For TDPa, the value is essentially equal to that of the ISCO, while both QDPa and KDPa have smaller values, indicative of continued stress operating near or inside the ISCO.

In all three cases, the time-averaged accretion rate is constant with radius out to $r/M \simeq$ 7–10; in this sense, all three have achieved a quasi-steady state within $\simeq 4r_{\mathrm{ISCO}}$, where r_{ISCO} is the radial coordinate of the innermost stable circular orbit, $2.32M$ (the rise in $\dot{M}$ and L at large radius in TDPa is likely an artifact of the stronger magnetic field with which that simulation was begun; equilibration takes place on timescales proportional to the local orbital period, which is, of course, $\propto r^{3/2}$, so inflow equilibration is slower at large radius). However, the actual value of the accretion rate is significantly different in the three simulations. The time-averaged mass accretion rate is highest in QDPa, exceeding that of KDPg by about 30%, while $\dot{M}$ is lower in TDPa by more than a factor of 2 compared to QDPa.

Accretion is, of course, driven by angular momentum transport, which is largely due to magnetic torques. To support these torques, the shell-integrated electromagnetic angular momentum flux must increase outward, as the net torque on the matter is the divergence of the EM angular momentum flux. The dependence of the electromagnetic angular momentum flux on initial field topology is therefore similar to that of the mass accretion rate: it is consistently greater for KDPg and QDPa than for TDPa. The most significant difference between the KDPg and QDPa curves is that in the region near the ISCO, the electromagnetic angular momentum flux in KDPg becomes almost constant with decreasing radius; this effect has previously been seen in other simulations that begin with dipole magnetic field loops

(Krolik et al. 2005). In the other two cases, the EM angular momentum flux continues to decline inward.

The mean magnetic field strength and Poynting flux show a very similar dependence on initial field topology: QDPa and KDPg closely resemble each other, TDPa is somewhat weaker. In the toroidal case, the disk body average magnetic energy density is weaker by a factor of several than in the other two simulations, and decreases inward toward the horizon rather more rapidly. Correspondingly, the time- and volume-averaged β parameter was 11 in QDPa, 16 in KDPg, and 30 in TDPa (because this is a volume-average, the corona is weighted heavily in this statistic). The electromagnetic energy flux shows the greatest variation between models. $\langle |T_t^r|_{\text{(EM)}}(r)\rangle_F$ in KDPg is consistently larger than the value in QDPa: by a factor of two at $r/M = 10$ and a factor of six at $r/M = 1.65$. The value in TDPa is smaller still by a factor of $\sim 2 - 4$ at these same radii.

All these relations can be understood in a straightforward fashion: there is a nearly-constant ratio between the EM angular momentum flux (and therefore the accretion rate), the Poynting flux, and the magnetic field intensity. In Figure 3, we plot the ratios of $\dot{M}$, $\langle |T_t^r|_{\text{(EM)}}(r)\rangle_F$ and$\langle |T_\phi^r|_{\text{(EM)}}(r)\rangle_F$ to $\langle ||b||^2(r)\rangle_F$. The inter-simulation contrast in the means of these quantities falls by a factor of several from the plot of their absolute values (Fig. 2) to the plot of their ratios to $||b||^2$ (Fig. 3). Thus, we see that their primary dependence is on the magnetic field strength. Only in the ratio of the electromagnetic energy flux to magnetic field strength do we see any global variation between the field topologies: $\langle |T_t^r|_{\text{(EM)}}(r)\rangle_F$ in KDPg is consistently a factor of two above QDPa and TDPa. This contrast arises from the strong Poynting flux in KDPg associated with the slower-moving, bound portion of the funnel-wall outflow (as can be seen from Figure 10 of Krolik et al. 2005, see §4).

The behavior of the fluid-frame stress can be seen in Figure 4, which depicts its time-averaged vertically-integrated value as a function of radius. To compute this quantity, we project the stress tensor onto a local tetrad system in each cell and multiply by the fluid-frame cell volume, which is computed by a similar projection (Krolik et al. 2005). After integrating over the bound matter on that spherical shell, we normalize the result to the surface area that this finite-thickness shell occupies in the equatorial plane. We present the result in this form in order to compare with the conventional representation of the vertically-integrated stress given by Novikov & Thorne (1973), which is presented in these terms. The Novikov-Thorne fluid-frame stress, unlike ours, is *assumed* to be zero at and within the ISCO. In the figure, the Novikov-Thorne stress is normalized by the time-averaged value of the accretion rate in the simulation.

Outside the ISCO, the radial profile of the Maxwell stress is similar to the prediction of the Novikov-Thorne model, but in no case is there a roll-over in the value near the ISCO. As

has been noted previously for the initial dipole field topology (Krolik et al. 2005), the $r - \phi$ stress does not go to zero at the ISCO, but is continuous down to the event horizon. This is true for all three field topologies, at least in a time-averaged sense, although the amplitude of the stress declines as one goes from dipole to quadrupole to toroidal field topology. In the dipole case, the logarithmic gradient of the stress as a function of radius actually steepens as the accretion flow approaches the horizon.

As can be seen from Figure 2, this extra stress does reduce the specific angular momentum carried into the hole by the accretion flow. At the ISCO the accretion flow in the toroidal field simulation has $L \sim L_{ISCO}$ (where $L_{ISCO} = 2.1$ is the specific angular momentum of the ISCO) and the accretion flows in the dipole and quadrupole simulations have $L \sim 2.05$ (a change of $\sim 2.5\%$ compared to L_{ISCO}). Below the ISCO, L in the quadrupole and toroidal cases remains constant with decreasing r. In the dipole simulation, L decreases to ~ 1.98 at $r/M = r_{in}$, a decrease of $\sim 6\%$ compared to L_{ISCO}. The fall off in the dipole case below the ISCO is presumably due to the steepening of the Maxwell stress in this region.

As has been remarked in earlier papers Krolik et al. (2005), Gammie et al. (2004), when $a/M = 0.9$, the magnitude of the Maxwell stress (i.e., the electromagnetic angular momentum flux) is smaller than the angular momentum flux associated directly with matter ($\dot{M}u_\phi$) in the inner disk. It follows (as shown in Figure 3), that the mean accreted angular momentum per unit rest-mass is only slightly below the Novikov-Thorne value (i.e., u_ϕ at the ISCO). Nonetheless, this continuity in the stress is important for other reasons: because the dissipation is rather more centrally-concentrated than the stress, this additional stress can be significant in the disk heat budget; and the relative importance of the additional stress increases sharply for higher black hole spins.

Thus, we see that the initial magnetic field geometry makes relatively little qualitative difference to the character of the accretion flow. The sense of its (weak) influence is that the simulation beginning with a purely toroidal magnetic field results in a saturated field amplitude a factor of two smaller than those resulting from poloidal seed fields. The Poynting flux, electromagnetic angular momentum flux, and accretion rate scale in direct proportion to the magnetic field energy density.

In their study based on axisymmetric simulations, McKinney & Narayan (2007a) also found that certain disk properties are largely independent of the initial field configuration. They found that the shell-averages of magnetic field quantities within the bound portion of the accretion flow (strictly speaking, where $||b||^2 < \rho$) follow power-law distributions that are the same regardless of the initial field topology. For example, they found that the field amplitude $\langle ||b||(r) \rangle_S \propto r^{-1.3}$ from the ISCO out to about $r = 10M$. Integrating the same magnetic field quantities (magnetic field strength and the lab-frame projections of the CT-

fields) over the bound portion of the flow in our simulations reveals that these quantities do scale roughly as power-laws in radius, but with shallower gradients than as determined by McKinney & Narayan (2007a). In addition, we see a slow trend with field topology, as well as significant fluctuations in time: $\langle ||b||(r)\rangle_S \propto r^{-0.75\pm0.09}$ in simulation KDPg (where $\pm$ denotes 1 std. deviation about the time-average), $\langle ||b||(r)\rangle_S \propto r^{-0.67\pm0.08}$ in simulation QDPa, and $\langle ||b||(r)\rangle_S \propto r^{-0.58\pm0.09}$ in simulation TDPa. The contrast between our results and McKinney & Narayan (2007a) could result from a number of considerations: the initial torus configurations differed in their radial pressure and angular momentum profiles, and our simulations are fully three-dimensional, rather than axisymmetric. These scalings may or may not be universal, but they appear to have little to do with the jet. As we will shortly show in §4, jet properties differ strongly from one initial magnetic topology to another; it must be, then, that jets depend on other properties in addition to the current distribution in the disk.

3.2. Corona

De Villiers et al. (2003) noted that the main disk body is surrounded by a low density region where the magnetic and thermal energies are in approximate equipartition. This region was designated as the coronal envelope. In contrast to the main disk body, where poloidal fluid velocities are dominated by turbulence, the poloidal motions in the coronal envelope are smooth on small scales and create an outgoing, but bound, backflow.

Figure 5 displays the spatial distribution of the time- and azimuthally-averaged β parameter overlaid with contours of the gas density for each of the three different topologies. KDPg shows the familiar strongly-magnetized axial funnel and a corona with relatively large regions of $\beta < 1$. QDPa shows a lower level of magnetization in the funnel region, while TDPa has much larger regions with $\beta > 1$ overall. To quantify these impressions, we adopt a more precise definition of the corona than that given in De Villiers et al. (2003). We define it as those regions of *bound* material that lie outside of $\sqrt{2}$ density-scale heights from the mid-plane, that is those cells that satisfy both $-hU_t \leq 1$ and $\rho/\rho_{eq} \leq e^{-2}$, where ρ_{eq} is the equatorial density and we measure along curves of constant r.

Using this definition, we integrate over the corona and over time to compute the average total volume and mass fraction in the corona, the volume-averaged β parameter, and the mean fluid-frame thermal and magnetic energy per unit mass. These data are given in Table 1.

The coronal regions for all three simulations take up half or more of the total simulation

volume but contain only 5% of the mass. The volume assigned to the corona for KDPg is a smaller percentage compared to the other models, but KDPg also contains an unbound jet along the funnel axis, which is excluded from the corona by definition. Within the coronal volume, the average thermal and magnetic energies per mass are similar, with volume averaged β values of $\simeq$ 2–4.

Figure 6 plots the angular profiles of density $\langle \rho(\theta; r) \rangle_A$, gas pressure $\langle P(\theta; r) \rangle_A$, magnetic pressure $\langle \frac{1}{2}||b||^2(\theta; r) \rangle_A$ and β $\langle 2P/||b||^2(\theta; r) \rangle_A$ at $r = 10M$. All three magnetic topology cases have very similar density profiles in the disk body, but appear to differ in the corona. Although our averaging period of $6000M$ is 30 orbital periods at the radius shown ($r = 10M$), it is not long enough to erase completely fluctuations in the coronal density profile: observe that the quadrupolar case is the most extended in the "southern hemisphere" corona while the toroidal case is the most extended in the "northern hemisphere".

Consistent with the general behavior we have already emphasized, the gas and magnetic pressure profiles in the disk body are very similar in the dipolar and quadrupolar cases, but both pressures are rather smaller in the toroidal field case. Nonetheless, all three cases share one important property: the magnetic pressure is almost flat for several scale-heights around the midplane. This finding is consistent with results from shearing-box simulations with much better vertical resolution (Hirose et al. 2005; Krolik et al. 2007). In the corona, the magnetic pressure drops rapidly with height in QDPa and TDPa, but remains nearly constant in KDPg. In all three cases, the magnetic and gas pressures track each other closely, so that the β profiles in the three runs are very similar.

Figure 7 plots the angular profiles of the electromagnetic contributions to T^r_ϕ and T^r_t ($\langle |T^r_t|_{\text{(EM)}}(\theta; r) \rangle_A$ and $\langle |T^r_\phi|_{\text{(EM)}}(\theta; r) \rangle_A$ respectively) at two different radii, $r/M = 1.65$ and $r/M = 10$. At the larger radius, it should come as no surprise that the profile of magnetic pressure shown at that radius in Figure 6 accurately predicts the profile of these two electromagnetic quantities. At the smaller radius, as we have already shown (Fig. 2), the magnetic field is considerably more intense in the dipole case than in the other two, so both the electromagnetic angular momentum flux and energy flux follow suit.

To summarize this section, we have found that, just as for the main disk body, the character of disk coronae is only weakly dependent upon the initial field topology. There are modest quantitative contrasts of the same sort as seen in the disk body—dipolar and quadrupolar initial fields both create somewhat stronger magnetic fields on average than does initial toroidal field—but that is all.

4. Outflows

4.1. Global measures

The formation of unbound outflows, or jets, is one of the most striking features of the KD models (De Villiers et al. 2003), all of which were initialized with single-loop dipolar magnetic fields. These outflows generically have two components: a Poynting flux jet inside the axial funnel formed by the centrifugal barrier, and a sheath of much denser unbound gas moving outward at sub-relativistic speed along the funnel's outer edge. As described in Hawley & Krolik (2006), energy for the Poynting flux comes from the rotation of the black hole, in a manner closely related to the classical Blandford-Znajek mechanism. In the case of the Schwarzschild hole, the absence of black hole rotation means that the magnetic field in the funnel, although relatively strong, is mostly radial and carries no Poynting flux. The funnel wall jet, on the other hand, appears to be powered by the significant gas and magnetic pressure near the ISCO. The gas retains enough angular momentum to be excluded from the funnel and is squeezed outward along the centrifugal barrier.

In contrast, the three-dimensional quadrupole and toroidal field simulations have substantially weaker unbound outflows, if any. Figure 8 shows the time-averaged shell-integrals of the mass outflow rate $\langle \dot{M}(r) \rangle_F$, magnetic field strength$\langle ||b||^2(r) \rangle_F$; along with the electromagnetic energy flux, $\langle |T_t^r|_{\text{(EM)}}(r) \rangle_F$ and angular momentum flux $\langle |T_\phi^r|_{\text{(EM)}}(r) \rangle_F$ in unbound material between $r = 10M$ and $r = 100M$. The values in KDPg are 10–100 times larger than those in QDPa, whose outflow quantities are, in turn, an order of magnitude larger than those in TDPa. For example, the unbound mass outflow rate at $r = 100M$ in KDPg is $\simeq 25$ times that of QDPa, while the mass outflow rate in TDPa is 10 times smaller than in QDPa. The strength of the outflow is directly related to the strength of the funnel field. In KDPg the time-averaged funnel magnetic energy density is 20–400 times greater than in the quadrupole model, while the toroidal model is weaker by another factor of 10. The mean Poynting flux in KDPg is therefore ~ 100 times the Poynting flux for QDPa. In other words, unlike the qualitative similarity of the accretion flows produced by these different field topologies, the outflows differ dramatically. To understand better the origin of this sharp contrast, in the next section we focus more closely on exactly how field is introduced into the funnel, and how its magnitude is controlled.

4.2. Funnel Field Creation

We have seen that the strength of the Poynting flux jet is very sensitive to the initial magnetic field topology. Because the establishment of large-scale field within the funnel

appears to be critical to driving a jet with substantial Poynting flux, we devote the remainder of this section to a close examination of just how different magnetic topologies lead to different funnel magnetic fields, leaning heavily on high-resolution 2-d axisymmetric simulations.

4.2.1. Dipole Topology

We begin by analyzing the axisymmetric simulation whose initial condition has already been shown to produce a significant jet, the dipole. Figure 9 shows a time series of color plots of the β parameter overlaid with white contours depicting poloidal field lines. As the radial field is sheared, a toroidal field (visible in Fig. 9 through its effect on β) is created and amplified, leading to poloidal magnetic pressure gradients (De Villiers & Hawley 2003b). Because the initial radial field has opposite sign on opposite sides of the equatorial plane, the toroidal field created by the shear also changes sign across the equator. The inner edge of the torus begins to move inward toward the event horizon, dragging the magnetic field with it. As the gas moves inward, its rotation velocity increases, further strengthening the toroidal field. As the magnetic pressure increases, gas is forced toward the equator where the field is comparatively weak, bringing the regions of oppositely-directed toroidal field closer together (see, e.g., the panel illustrating $t = 800M$). As a result, a strong current sheet forms along the equatorial plane.

Once the inner edge of the accretion flow arrives at the black hole ($t \sim 700M$), field lines attach to the event horizon, and gas rapidly drains off them. Field lines slide toward the poles as they expand outward at relativistic speed, driven by the contrast between the high magnetic pressure near the equatorial plane and the much lower pressure higher up along the axis. This flow moves outward so swiftly because it is almost entirely unencumbered by the inertia of matter. As discussed in Hawley & Krolik (2006), a magnetic tower forms, similar to the one predicted on analytic grounds (Lynden-Bell 2003) and seen in other simulations (Kato et al. 2004). However, in contrast to these models, tightly-wrapped field lines persist only briefly; the large vertical gradient in magnetic pressure propels the upper loops so rapidly outward that in the steady-state the field lines are better described as loosely helical than as a tightly-wrapped coil. The radial field inside the funnel has the same sign as the vertical component of the initial dipole loop inside the initial pressure maximum; these field lines close outside of $r = 100$M, reentering the problem volume throughout the corona.

A time history of the unbound Poynting flux at $r = 100M$, normalized by the instantaneous (coordinate frame) magnetic field energy within the bound accretion flow, is shown in Figure 10 for both the three-dimensional simulation KDPg and the high-resolution axisymmetric model. In both cases, once the jet is established (a process taking $\lesssim 1000M$), the

Poynting flux jet persists. It is frequently perturbed, and the amplitude undergoes fluctuations, but its basic properties persist throughout the simulation. Excluding initial transients (i.e. $t < 1500M$), the jet histories of the two simulations are very similar to one another, despite the differences in dimensionality, (poloidal) resolution, torus configuration and equation of state: in both cases, the ratio of jet EM luminosity to energy density in magnetic energy is $\simeq 0.1$–0.2 per time-unit. This similarity demonstrates that, for this topology at least, the properties of the funnel field depend primarily on the field strength within the initial accretion flow, and that funnel field creation is a primarily axisymmetric process.

Although the initial magnetic field had structure only on the scale of the disk thickness, the *essentially laminar* dynamics of initial inflow lead quickly to the formation of truly large-scale field. On the other hand, because the accretion flow takes longer to be established than the jet does, the magnetic field in the funnel acts in effect as a permanent boundary condition for the accretion flow. In other words, these simulations mimic the long-term behavior of an accretion flow in which there is large-scale net magnetic flux threading the event horizon and filling a cone around the axis, but no large-scale flux piercing the disk proper. As both the three-dimensional and two-dimensional simulations demonstrate, it is entirely possible for long-term quasi-stationary accretion to coexist with a strong Poynting flux jet whose foundation is magnetic flux trapped long before.

4.2.2.   Quadrupole Topology

We next consider the evolution of an initial quadrupolar field in high resolution axisymmetry. Figure 11 shows a time series of plots illustrating β and the poloidal field line structure for this case. Initially, the loops of weak poloidal magnetic field enclose two regions, located above and below the pressure maximum (see Figure 1, center panel). In a similar fashion to the dipole case, these loops are sheared out, creating ever growing toroidal field and producing strong poloidal magnetic pressure gradients. In contrast to the dipole case, however, two current sheets are formed, one above the equatorial plane, one below. The magnetic pressure forces gas toward these current sheets, where the magnetic pressure has a local minimum.

As the inner edge of the torus moves radially inward toward the black hole, the current sheets maintain their structure. When the field reaches the black hole, the current sheets are located above and below the equator. As with the dipole, gas drains off the field lines, which anchor themselves in the event horizon, and the field lines between the current sheets and the axis slide toward the poles, where the density and pressure are very low. These field lines expand outward relativistically, filling the funnel region and establishing a large-scale

quadrupole field.

While this field is in place it supports a Poynting-flux jet, but the power in the jet is significantly less than that in the axisymmetric dipolar simulation. Averaged from $t = 2800M$ to $t' = 3800M$, the EM flux in the dipolar case is twice as strong as in the quadrupolar simulation when measured at $r = 10M$, and 10 times stronger measured at $r = 100M$ (we will discuss later why the contrast was more than an order of magnitude greater in the 3-d simulations). Figure 12 compares the dipole jet Poynting flux with that of the quadrupole simulation as a function of time at $r = 100M$, normalized by the total magnetic field energy in the disk. In terms of this normalized power, the jet in the quadrupole simulation is a factor of 2–10 weaker than that associated with dipole model; in other words, much of the actual power contrast between the dipolar and quadrupolar cases can be explained in terms of a reduction in this "magnetic efficiency". Unlike the situation for accretion properties, contrasts in jet luminosity from one topology to another cannot be described solely in terms of contrasts in mean magnetic field strength.

McKinney & Gammie (2004) reported that replacing the dipole with a quadrupole field led to a jet that is weaker by a factor of 2–3, but for several reasons one should expect only qualitative, not quantitative agreement with our results. They measured the jet luminosity at $r = 40M$ and their initial pressure maximum was much closer to the black hole ($r = 12M$), so that the radial dynamic range of their genuine accretion flow was considerably smaller. Their disk was also geometrically thicker, partly because their code solved a total energy equation, and partly because their initial state was hotter.

Simple geometry accounts for the qualitative contrast between the jet produced by an initially quadrupolar magnetic geometry and that driven by an initially dipolar field. In the quadrupolar case, relatively small amplitude vertical oscillations in the inner region of the accretion flow can lead to reconnection between magnetic field in the funnel and magnetic field in the disk because vertical field of both signs is available in the same hemisphere. The result is to break the magnetic connection between the black hole horizon and large radius. Put another way, the presence of closed field loops on the same side of the equator offers the opportunity for easy collapse of these loops to zero. In the dipole case, however, the sign of the vertical magnetic field passing through the equator is the same everywhere inside $r = 25M$.

The net result of this geometric contrast is that, while quadrupolar field configurations can pump magnetic field into the outflow funnel and support a jet, they can also equally easily destroy such a jet by reconnection with oppositely-directed field. Jets in this case are consequently very unsteady, and exhibit strong variability in the Poynting flux, as shown in Figure 12. This variability is a major factor in depressing the time-averaged EM luminosity

of jets driven by quadrupolar fields.

Because the code simulates the equations of ideal MHD, reconnection is numerical and occurs at the grid scale. As such, the reconnection rate is resolution dependent (lower resolution promotes reconnection). We cannot therefore make specific predictions regarding the variability characteristics of jets in Nature, as this is determined (in our simulations at least) by competition between processes that are physical in character (e.g., orbital dynamics, magnetic forces) and purely numerical (the reconnection rate).

The rate of reconnection is also determined by details of the field geometry, in addition to its basic topology. To investigate this sort of dependence, we have conducted a series of lower resolution (256^2) axisymmetric quadrupolar simulations in which we varied the size of the initial torus, and hence the scale of the initial field loops. We kept the inner edge of the torus fixed at $r = 15M$, but reduced the angular momentum ℓ in order to reduce the vertical thickness of the torus, and consequently reduce the vertical extent of the quadrupolar loops. Simulations were carried out for a variety of values of ℓ, ranging from $\ell = 4.9$ to $\ell = 5.2$ in steps of $\ell = 0.05$.

For the purposes of our discussion here, we focus on the $\ell = 4.9$ torus, which serves to illustrate the impact of vertical scale height on the evolution of the quadrupole topology. Specifically, setting $\ell = 4.9$ results in a torus which is initially a factor of two thinner (in terms of the density scale height, measured along surfaces of constant radius at the location of the pressure maximum) than the $\ell = 5.2$ torus previously discussed. The vertical thickness of the resulting quadrupolar field loops is then very similar to that of loops in the sub-Keplerian torus used in QDPa.

The initial evolution of this system is shown in Figure 13. The evolution proceeds as before: current sheets form above and below the equatorial plane as the inner edge of the torus moves toward the black hole. This time, however, the two current sheets are much closer to the equatorial plane (contrast Fig. 13 with Fig. 11). Around $t = 800M$ the current sheets buckle, apparently due to an instability, and the coherent poloidal field structure is destroyed. A similar phenomenon was observed in QDPa, which had a similar scale-height: the current sheets destabilized far from the black hole, destroying the coherent poloidal field structure. As a result, no large scale poloidal field was dragged into the near horizon region by the torus, and the resulting field inside the funnel region is substantially reduced. We note that in three-dimensions the presence of non-axisymmetric MRI modes are likely to enhance the rate of reconnection, further decreasing the likelihood that an organized quadrupole configuration will survive to create a significant funnel field.

These additional simulations show that the strength of Poynting-dominated jets depends

on field geometry in two senses: it is topology-dependent and shape-dependent. Quadrupolar magnetic topology leads to easier reconnection, and therefore weaker funnel fields and jets, than does dipolar topology, and geometrically thinner quadrupole loops make reconnection still more rapid.

4.2.3. Multiple Loop Topology

We have shown how large dipolar loops can create strong jets, but what happens if the oppositely-directed vertical field on the far side of the loop is accreted? This did not occur in KDPg, in part because it did not run long enough and in part because the finite mass in our torus meant that the matter outside the pressure maximum moves outward over time, not inward. In a real accretion disk, however, continuing mass re-supply will force the far sides of even large dipolar loops to accrete.

To explore this sort of event, we ran a two-dimensional simulation whose initial state contained a series of four narrow dipolar loops (described in §2). The initial evolution of this topology is shown in Figures 14 and 15. The first of these figures shows the descent of the innermost radial loop into the near-horizon region and the establishment of a Poynting flux jet. The second figure shows the descent of the second (moving out in radius) of these loops and its interaction with the field structures established by the first loop.

Over the timescale considered, the evolution of this model is determined by the two innermost loops, both initially inside the pressure maximum (see Fig. 1). As for a single dipole loop, the first loop forms a funnel dipole field by $t = 700M$. However, its shape differs significantly from the single loop because the second loop begins its descent toward the inner disk even before the inner edge of the first loop nears the event horizon (Fig. 14). As the second loop moves inward, it displaces the field lines of the first loop, forcing the midplane portions of the outer half of the first loop inward, and the off-plane portions of the first loop to higher altitude at their original radius. The result is that the first loop is very nearly transformed into a pair of loops, one on each side of the midplane. After arriving in the inner disk, the field of the second loop expands rapidly toward the funnel region. It pushes on the almost closed sections of the first loop, triggering rapid reconnection where its oppositely-directed segments pass very close to one another at small radius (Fig. 15). At this point, the transformation of the first loop into a disconnected quadrupolar loop pair is complete, and the loops fly off to large distance, emptying the funnel of magnetic field. The funnel is then refilled with flux from the second loop. These dramatic events are mirrored in the very large fluctuations in normalized Poynting luminosity shown in Figure 12. Jumps in output even greater in relative terms than those displayed by the quadrupolar simulation are frequent,

and can be associated with these episodes of funnel field establishment and annihilation. Note that while the multiple-loop jet is highly variable, similar to the quadrupolar jet, the instantaneous strength of the Poynting-flux jet (when it is strong) is similar to that of model KDPg when normalized for disk magnetic field strength. In this sense, the "efficiency" of these systems in using magnetic field generated in the disk for jets appears to be a function of poloidal field character, declining as the relative importance of higher multipole moments increases.

In interpreting this simulation, it is important to bear in mind that, unlike any of the others reported in this paper, its accretion flow never achieves anything resembling a quasi-stationary state. The multiple loop structure also requires high resolution to prevent reconnection from occurring at too rapid a rate. It is for this reason that, unlike the large dipolar loop and quadrupolar caess, we report no 3-d simulation results for this field geometry. Thus, we can be less confident than in the other cases that the specific phenomenology we observe may be associated with real systems in a state of continuing accretion. What it *does* demonstrate, however, is that accretion of a series of closed dipolar loops can lead to a sequence of field establishment and destruction rather similar to what was seen in the quadrupolar case, and through mechanisms that also resemble those seen when the initial field is quadrupolar. It also supports our qualitative inference that maintenance of a consistent sign of vertical field is essential to the long-term support of a Poynting-dominated jet. The lifetime for an episode of strong outflow is roughly the inflow time for the outer anchor point of the loop.

4.2.4. Toroidal Field Topology

In the poloidal cases, magnetic field is injected into the funnel by strong toroidal field pressure in the plunging region. One might expect that this process could act equally efficiently when the magnetic field is toroidal from the start. If the toroidal field has a consistent sign, the radial component created when it expands outward would also have a consistent sign, satisfying the coherent vertical field criterion we have inferred from study of the poloidal simulations. If so, the toroidal field case should also drive a powerful jet. However, it does nothing of the sort.

Figures 16 – 17 are a series of snapshots of the β parameter and the radial field structure in the evolving torus of simulation TDPa. In contrast to the poloidal loop simulations, there is no initial radial field to generate toroidal field through shear. Instead, the evolution is governed entirely by the development of the nonaxisymmetric MRI. The fastest-growing modes for the MRI in this context have large k_z and azimuthal wavelength $\sim v_A/\Omega$, which is

much shorter than the disk thickness when the field is weak (Balbus & Hawley 1992). The magnetic structures that develop are then predominantly on short lengthscales. Note the rapid spatial variation in sign in the radial field in Figure 17. With time, the radial field features become somewhat more radially elongated, but field lines do not connect extended regions; no large-scale coherent poloidal field is generated from the initial toroidal field. Magnetic field amplification is less than in the poloidal field initial conditions, and β never becomes less than 1 near the hole. Matter tends to remain with the field rather than drain either into the hole or toward a localized region such as the equator, as seen in the dipole case. Any vertical expansion of the field would therefore have to overcome the inertia of the matter and, as can be seen from Figure 17, this does not occur.

The absence of a funnel-field in the toroidal topology follows directly from the specific properties of the toroidal field MRI: the poloidal fields created by the MRI are typically small scale. No radially-extended poloidal field connects the near horizon region to the disk. What radial field there is is accreted faster than it can tap into the differential rotation and generate strong near-hole fields. The main disk-body in the toroidal case remains gas pressure-dominated at all times, and there are no strong magnetic pressure gradients to drive an expansion of the field into the funnel region. The absence of a funnel field means there is no Poynting flux jet.

It appears, then, that creation of a strong funnel field, and therefore a strong Poynting jet when the black hole spins rapidly, depends essentially on the existence of some coherent poloidal field in the initial state. Purely toroidal field initial conditions can lead to short coherence-length poloidal loops with rapidly alternating sign, but no large-scale poloidal field components.

5. Summary and Conclusions

Through a series of numerical studies, we have examined the influence of the initial field topology on the properties of magnetized black hole accretion flows. In particular, we have performed full three-dimensional simulations of three different initial field topologies: a large-scale dipolar loop, a pair of quadrupolar loops separated by the equatorial plane, and a purely toroidal field. Apart from the imposed initial field topologies, the initial conditions used in each of these simulations were identical: a $\Gamma = 5/3$ hydrostatic torus with a slightly sub-Keplerian distribution of angular momentum around a rotating $(a/M = 0.9)$ black hole. The two poloidal field topologies were evolved to $t = 10000M$, while the toroidal case was evolved to $t = 29000M$.

De Villiers et al. (2003) described the late-time structure of the resulting accretion flow in terms of distinct components: the main disk body, the coronal envelope, and an unbound outflow which itself could be separated into a matter-dominated funnel-wall jet and a Poynting-flux jet in the funnel interior. We have found that the late-time averaged properties of the main disk body exhibit only modest quantitative contrasts attributable to different initial field topologies: the dipolar and quadrupolar cases are roughly similar, and both create somewhat stronger magnetic fields than the toroidal case. So long as there is some weak magnetic field present, the MRI generates turbulence and drives accretion, although the character of the purely toroidal MRI is somewhat different from that produced by poloidal fields. Because the Maxwell stress controls the surface density required to support a given accretion rate, and the cascade of energy to smaller scales in the MHD turbulence leads ultimately to disk heating, we expect that the radiation emitted by the disk will likewise be only weakly dependent on magnetic topology. It is possible that different magnetic topologies could produce different vertical profiles of dissipation (which these simulations are not designed to study), but the similarity in magnetic pressure profiles (Fig. 6) suggests that even those differences are likely to be minor.

In regard to the accretion flow, we found only two dependences on field topology worth noting: for fixed outer torus mass, the initial toroidal field simulation gives a somewhat lower accretion rate (a result foreshadowed in Hawley & Krolik 2002). In addition, the magnetic field in the plunging region is, in relative terms, somewhat stronger in the large dipolar loop case than for quadrupolar or toroidal fields, so that stresses near the ISCO are somewhat stronger when the field topology is dipolar. In other words, the short-wavelength behavior of the MRI-driven MHD turbulence in the disk produces near-universal behavior, independent of magnetic field structure.

Jets are quite different. *Laminar* flow dynamics can, given the right conditions (e.g., the right field topology), inflate field with no pre-existing structure on scales larger than a disk scale-height into a truly global field. Simulations that begin with a large dipole loop in the initial torus produce a strong Poynting-flux jet in the axial funnel and a comparably strong matter-dominated funnel-wall outflow. The inner field lines of the dipolar loop move quickly inward to fill the funnel, and remain there until the opposite side of the loop is accreted, an event which may not happen until quite a long time later. Thus, this case mimics a situation in which net magnetic flux has been trapped against the black hole event horizon by previous accretion. When this trapped flux creates a coherent poloidal field in the funnel, the black hole's spin forces nearby field lines into rotation and drives a large outward-directed Poynting flux.

This sequence of events is not as easily achieved with any of the other field geometries

we explored. Unlike the dipole configuration, the quadrupole features a pair of current sheets located above and below the equator. These current sheets are subject to instabilities that can lead to reconnection in the magnetic field and loss of extended field coherence. Even when the quadrupole is successful in establishing a funnel field, the jet may live only briefly because fluctuations in the accretion flow can generate reconnection events. By the same token, quadrupolar field can also restore field to an empty funnel. Consequently, any jet based on quadrupolar field tends to be unstable and episodic, with the timescale and amplitude of changes set both by details of the field geometry and the rate of reconnection. Unfortunately, it is very hard to obtain any information about the former in real systems, and in our simulations the latter is controlled by numerical effects and resolution, so it is impossible for us to make predictive statements about the timescale or amplitude of jet variability in this case.

All of the models reported on above used a black hole with a spin $a/M = 0.9$. To test our conclusions against other black hole spins we also ran two three-dimensional initially quadrupolar simulations with black hole spins $a/M = 0.0$ and, $a/M = 0.998$. The effect of a wide range of black hole spins (including a counter-rotating hole) on dipolar models was studied by Hawley & Krolik (2006). No Poynting flux jet is present for a Schwarzschild hole regardless of the initial field topology. The energy to drive the Poynting flux originates with the spin of the hole. However, the funnel is still filled with radial field, which is considerably stronger in the dipole case compared to the quadrupole. On the other hand, the funnel field strength increases with black hole spin for a given field topology. For the rapidly-spinning hole, the Poynting flux jet is stronger than in the $a/M = 0.9$ simulations for both topologies, but as we have discussed, it is considerably weaker when the initial field is quadrupolar than when it is dipolar. Specifically, the ratio between the time-averaged Poynting luminosity with dipolar field to the Poynting luminosity with quadrupolar field is ~ 350 for $a/M = 0.998$ and ~ 335 for $a/M = 0.9$. Thus, the accretion dynamics control what sort of field is brought to the vicinity of the black hole and fill the funnel, and the black hole spin determines how energetic the resulting jet is.

The purely toroidal field topology does not generate any jet at all. The only way for toroidal field to create any poloidal field is by initiating non-axisymmetric perturbations of alternating sign. The lengthscales of these perturbations must be relatively short, and the portions of opposite sign must balance in magnitude. Fields of this sort can do very little to fill the funnel region because they are even more subject to reconnection than is the quadrupolar field.

When the initial field is a single dipolar loop that wraps around the initial pressure maximum of the simulation, all the vertical field brought down to the funnel by the initial

accretion has the same direction. In real disks containing closed dipolar loops, oppositely directed vertical field will, sooner or later, arrive in the inner disk, and it may cancel the funnel field. To investigate this possibility, we ran a high-resolution axisymmetric simulation that began with four narrow dipolar loops within the initial torus. Its subsequent evolution qualitatively supports this conjecture. The innermost loop produces a funnel field as in the single dipole loop model. When the second loop, oriented oppositely from the first one, descends, it displaces the field established by the first loop. The funnel field established by the first loop reconnects, detaches from the event horizon, and is rapidly expelled from the grid. The second loop then expands poloidally and reestablishes the funnel field. In other words, the accretion of dipolar field loops leads to jet creation, but its structure is highly-variable: the narrower the dipolar loops present in the accretion flow, the more variability we can expect in the jet.

When a simulation is initialized with (possibly multiple) dipolar field loop(s) that cross the equatorial plane, the strength of the resulting Poynting-flux jet depends on the strength of the magnetic field within the disk itself and on the spin of the hole. Poynting-flux jets that are formed from quadrupolar fields are generically much weaker than their dipolar counterparts, even when magnetic field strength in the disk body is taken into account. How much weaker depends on other factors as well, including disk thickness, location of the inner edge of the initial torus, and numerical resolution. In the limited range of numerical experiments reported here, we have seen suppression factors ranging from several to several hundred.

Real accretion flows are likely to have a mixture, possibly time-varying, of all these field topologies. Real jets from black holes will exhibit behavior combining the sorts of events we have seen in this paper: stability over longer timescales when the field is mostly made of large dipolar loops, greater variability and occasional jet quenching when the field has a larger contribution from higher multipoles, jet elimination when the field is mostly toroidal. It is possible that in addition to the sort of coherent funnel field spontaneously created by large closed-loop poloidal structures, there is a large-scale field imposed by external boundary conditions. We plan to investigate the impact of such an externally-imposed field in future work.

This study is only one small step in the process of exploring the mechanisms to create large scale field configurations within accretion flows. Here the large scale field formation process we have observed results from an interaction between poloidal field components in the accretion flow and the boundary represented by the black hole. The mechanism operates in axisymmetry as well as in three dimensions, so it is not a dynamo if that word is defined as in the antidynamo theorem. Many authors have conjectured that an inverse cascade within the

three dimensional turbulent disk itself might generate large scale fields; we see no evidence in these simulations of any disk field with structure on scales more than a few scale-heights, but we caution that the resolution limitations of three dimensional global simulations make this observation less than definitive.

The results we have reported also stimulate speculations about whether the contrasts in jet phenomenology from one object, or class of objects, to another is due in part to differences in the mixture of different field topologies, or the interaction of different topologies in the flow. For example, could the jet outbursts sometimes seen in Galactic black hole binaries when they cross the "jet line" (Remillard & McClintock 2006) be due to rapid field annihilation and loop expulsion of the sort observed in the multiple dipolar loop simulation? Perhaps the radio-weakness of most AGN (see e.g. White et al. 2007) is due to the predominance of small-scale multipolar field in their accretion flows as a result of accreting from a turbulent interstellar medium? As we learn more about how it acts, we may find that magnetic topology can, in fact, be inferred from phenomenology.

REFERENCES

Balbus, S. A., & Hawley, J. F. 1992, ApJ, 400, 610

—. 1998, Reviews of Modern Physics, 70, 1

Blandford, R. D., & Payne, D. G. 1982, MNRAS, 199, 883

Blandford, R. D., & Znajek, R. L. 1977, MNRAS, 179, 433

De Villiers, J., & Hawley, J. F. 2003a, ApJ, 589, 458

—. 2003b, ApJ, 592, 1060

De Villiers, J., Hawley, J. F., & Krolik, J. H. 2003, ApJ, 599, 1238

De Villiers, J., Hawley, J. F., Krolik, J. H., & Hirose, S. 2005, ApJ, 620, 878

De Villiers, J.-P. 2006, ArXiv Astrophysics e-prints, astro-ph

Gammie, C. F. 1999, ApJ, 522, L57

Gammie, C. F., Shapiro, S. L., & McKinney, J. C. 2004, ApJ, 602, 312

Hawley, J. F., & Krolik, J. H. 2002, ApJ, 566, 164

—. 2006, ApJ, 641, 103

Hirose, S., Krolik, J. H., De Villiers, J., & Hawley, J. F. 2004, ApJ, 606, 1083

Hirose, S., Krolik, J. H., & Stone, J. M. 2005, ArXiv Astrophysics e-prints

Jackson, J. D. 1975, Classical electrodynamics (92/12/31, New York: Wiley, 1975, 2nd ed.)

Kato, Y., Mineshige, S., & Shibata, K. 2004, ApJ, 605, 307

Krolik, J. H. 1999, ApJ, 515, L73

Krolik, J. H., Hawley, J. F., & Hirose, S. 2005, ApJ, 622, 1008

Krolik, J. H., Hirose, S., & Blaes, O. 2007, ApJ, 664, 1045

Lynden-Bell, D. 2003, MNRAS, 341, 1360

McKinney, J. C., & Gammie, C. F. 2004, ApJ, 611, 977

McKinney, J. C., & Narayan, R. 2007a, MNRAS, 375, 513

—. 2007b, MNRAS, 375, 531

Moffatt, H. K. 1978, Magnetic field generation in electrically conducting fluids (Cambridge, England, Cambridge University Press, 1978. 353 p.)

Novikov, I. D., & Thorne, K. S. 1973, in Black Holes: Les Astres Occlus, ed. C. DeWitt & B. DeWitt (New York; Gordon and Breach)

Remillard, R. A., & McClintock, J. E. 2006, ARA&A, 44, 49

White, R. L., Helfand, D. J., Becker, R. H., Glikman, E., & de Vries, W. 2007, ApJ, 654, 99
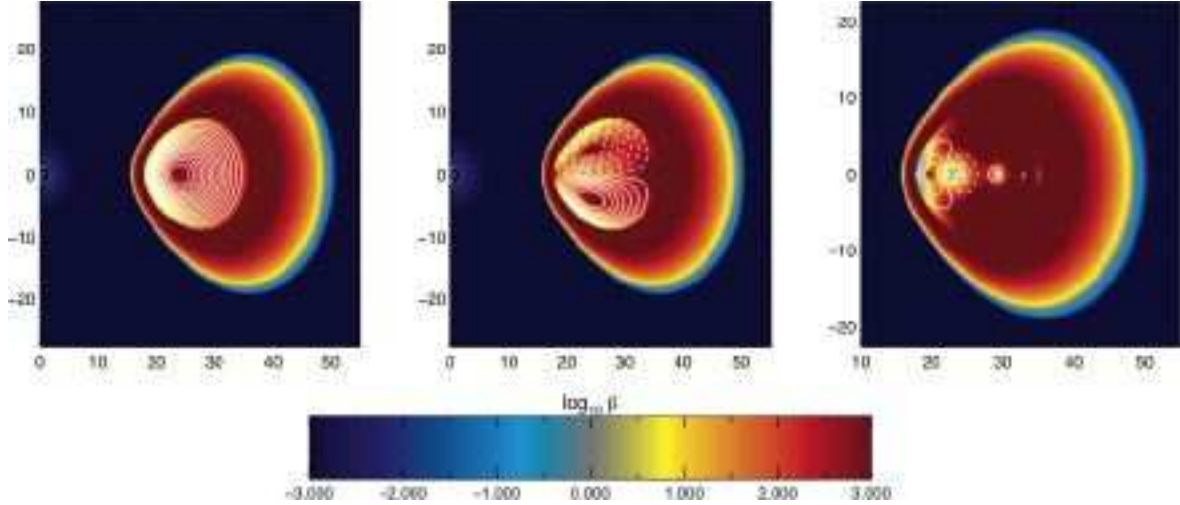
Fig. 1.— Initial configurations of dipole (left panel), quadrupole (center panel) and multiple loop (right panel) field topologies. The torus for the multiple loop topology is shown slightly zoomed to illustrate better the initial field structure. White contours denote magnetic field lines, color contours the gas β parameter. Solid versus dashed lines indicate field polarity; solid lines denote current into the page, dashed lines current out of the page.

Table 1.   Coronal Diagnostics

Model	$\langle M_c \rangle_V / \langle M_{tot} \rangle_V$	$\langle \beta_c \rangle_V$	$\langle E_c^{\mathrm{therm}} \rangle_V / \langle M_c \rangle_V$	$\langle E_c^{\mathrm{mag}} \rangle_V / \langle M_c \rangle_V$	$\langle \mathrm{Vol}_c \rangle_V / \langle \mathrm{Vol}_{tot} \rangle_V$
KDPg	0.055	3.6	2.9×10^{-3}	1.1×10^{-3}	0.48
QDPa	0.050	2.1	2.7×10^{-3}	1.8×10^{-3}	0.59
TDPa	0.054	3.4	2.5×10^{-3}	1.0×10^{-3}	0.61

Note. — Subscript "c" denotes volume integral over the coronal region (as defined in the text), whereas subscript "tot" denotes volume integral over the total simulation region.
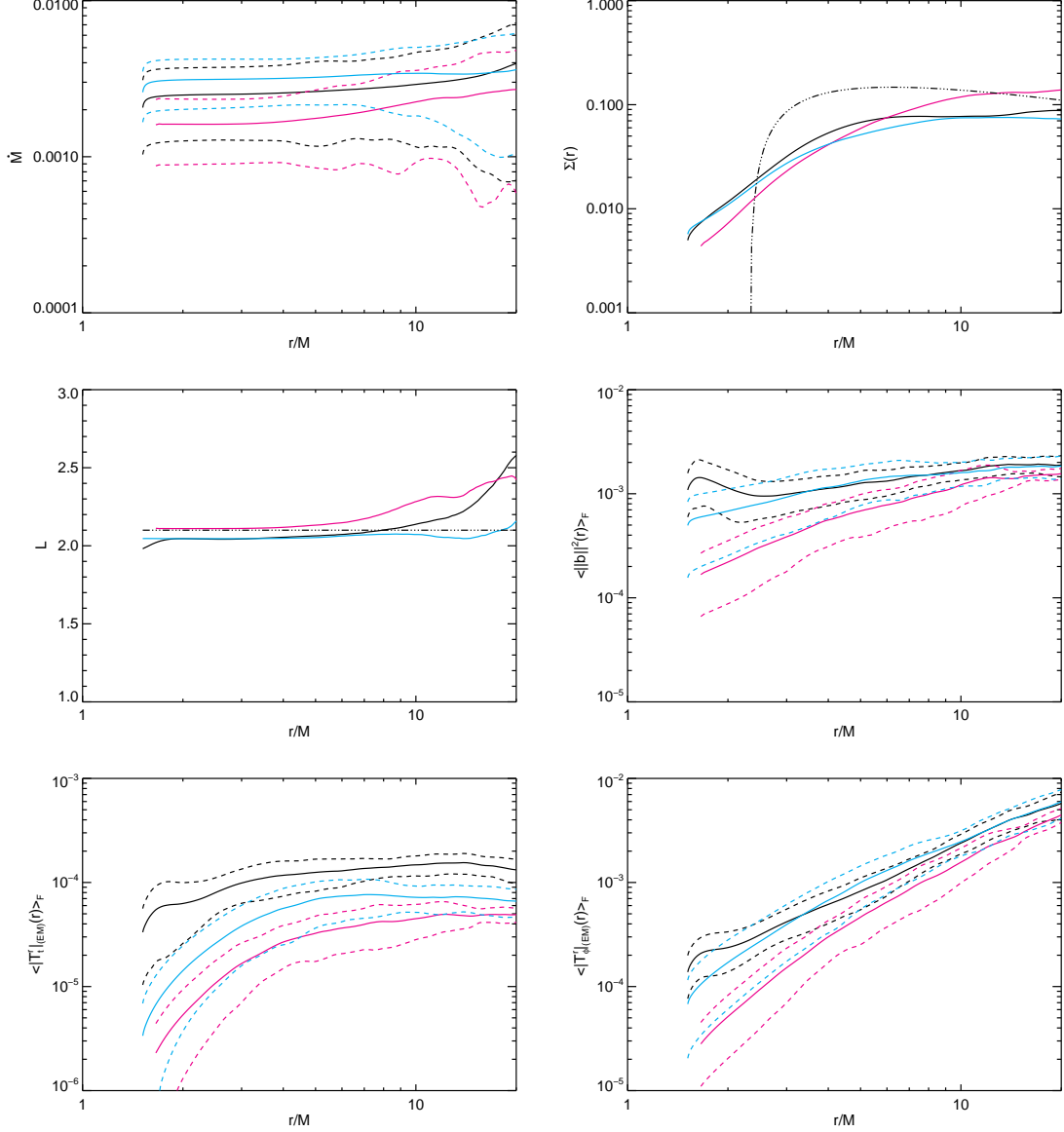
Fig. 2.— Time-averaged, shell-integrals of the accretion rate, $\dot{M}$ (top left panel), surface density $\Sigma(r)$ (top right panel, dot-dash lines show the surface density distribution predicted by Novikov & Thorne 1973), the net accreted angular momentum per unit rest mass, L, (center left panel; dot-dashed line indicates value at the ISCO), magnetic energy density $\langle ||b||^2(r)\rangle_F$ (center right panel); the electromagnetic contribution to the energy flux $\langle |T^r_t|_{(EM)}(r)\rangle_F$ (bottom left panel) and angular momentum flux $\langle |T^r_\phi|_{(EM)}(r)\rangle_F$ (bottom right panel) in bound material. Each figure shows data from KDPg (black lines), QDPa (blue lines) and TDPa (magenta lines) time-averaged over $4000-10000M$ for KDPg and QDPa, and $12500-18500M$ for TDPa. Solid lines denote the time average, dashed lines (where shown) ± 1 standard deviation from the average. Note that the radial coordinate of the ISCO is $2.32M$ for the black hole spin $a/M = 0.9$.
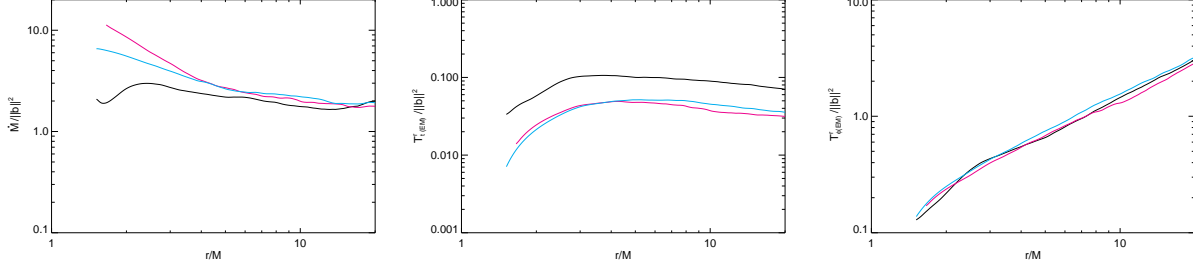
Fig. 3.— Time-averaged ratio of the accretion rate $\dot{M}$ (left panel), the electromagnetic contribution to the energy flux $\langle |T^r_t|_{(EM)}(r)\rangle_F$ (center panel) and angular momentum flux $\langle |T^r_\phi|_{(EM)}(r)\rangle_F$ (right panel) to the magnetic field strength $\langle ||b||^2(r)\rangle_F$; all are restricted to bound material. Each figure shows data from KDPg (black lines), QDPa (blue lines) and TDPa (magenta lines). The time-averaging is over the period $4000 - 10000M$ for KDPg and QDPa, and $12500 - 18500M$ for TDPa.
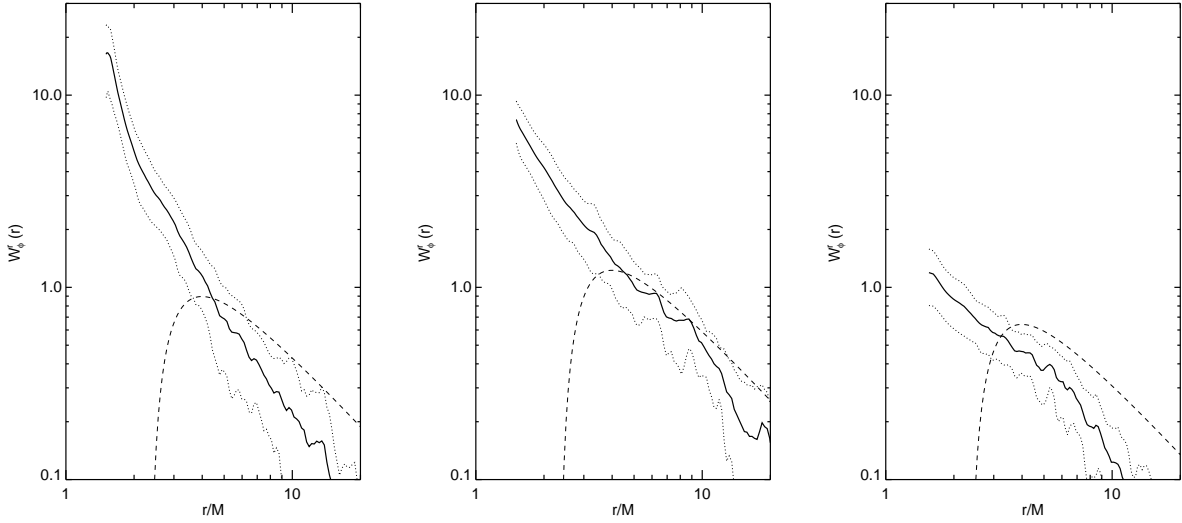
Fig. 4.— Time-averaged fluid-frame Maxwell stress, $\mathcal{W}^{(r)}_{(\phi)}$ (solid lines) for simulations KDPg (left panel), QDPa (center panel) and TDPa (right panel). Solid lines denote the time average, dotted lines ± 1 standard deviation from the average. The Novikov-Thorne prediction of the fluid-frame stress for a thin disk with an accretion rate equal to the time-average for that simulation is shown with a dashed line. KDPg and QDPa are averaged over 8000–10000M and TDPa is averaged over 2–$2.2 \times 10^4 M$.
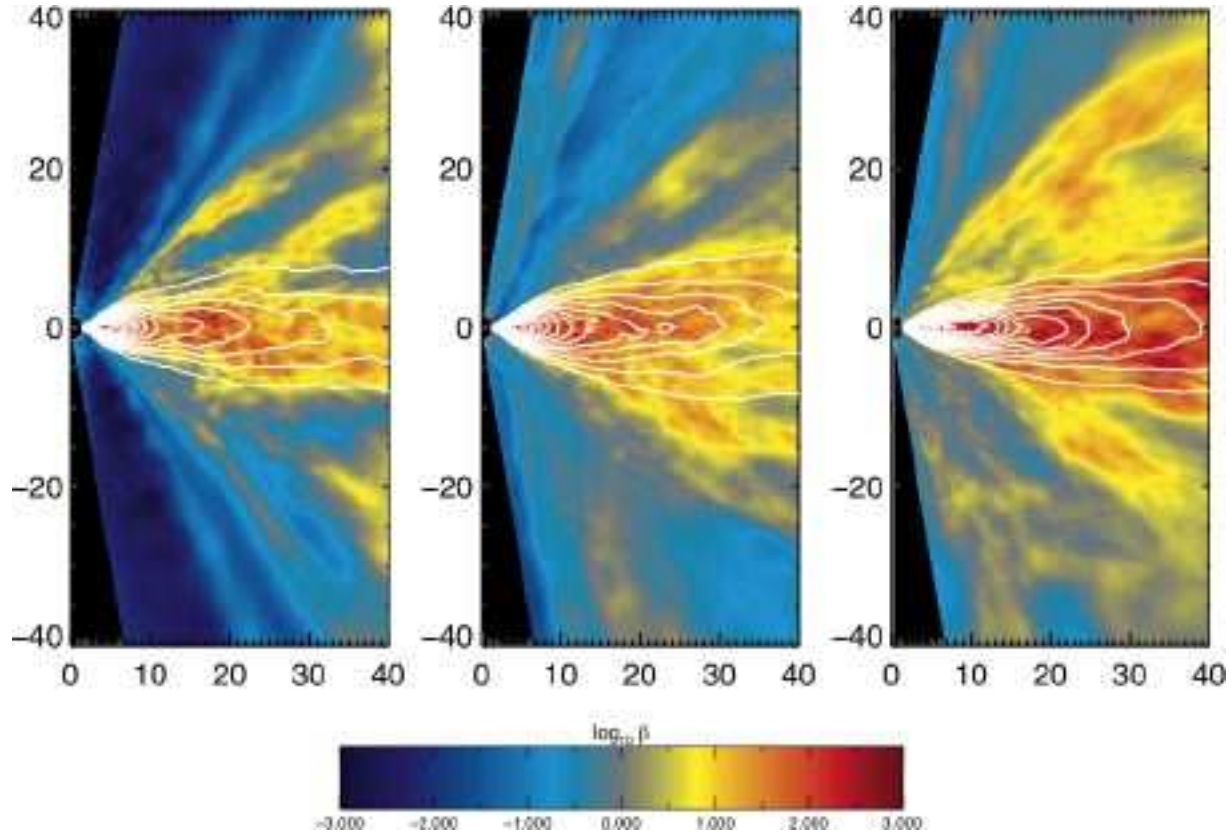
Fig. 5.— Color contours of the time- and azimuthally-averaged β parameter for simulations KDPg (left panel), QDPa (center panel) and TDPa (right panel), overlaid with white contours of gas density. KDPg and QDPa are averaged over 8000–$10000M$ and TDPa is averaged over 2–$2.2 \times 10^4 M$.
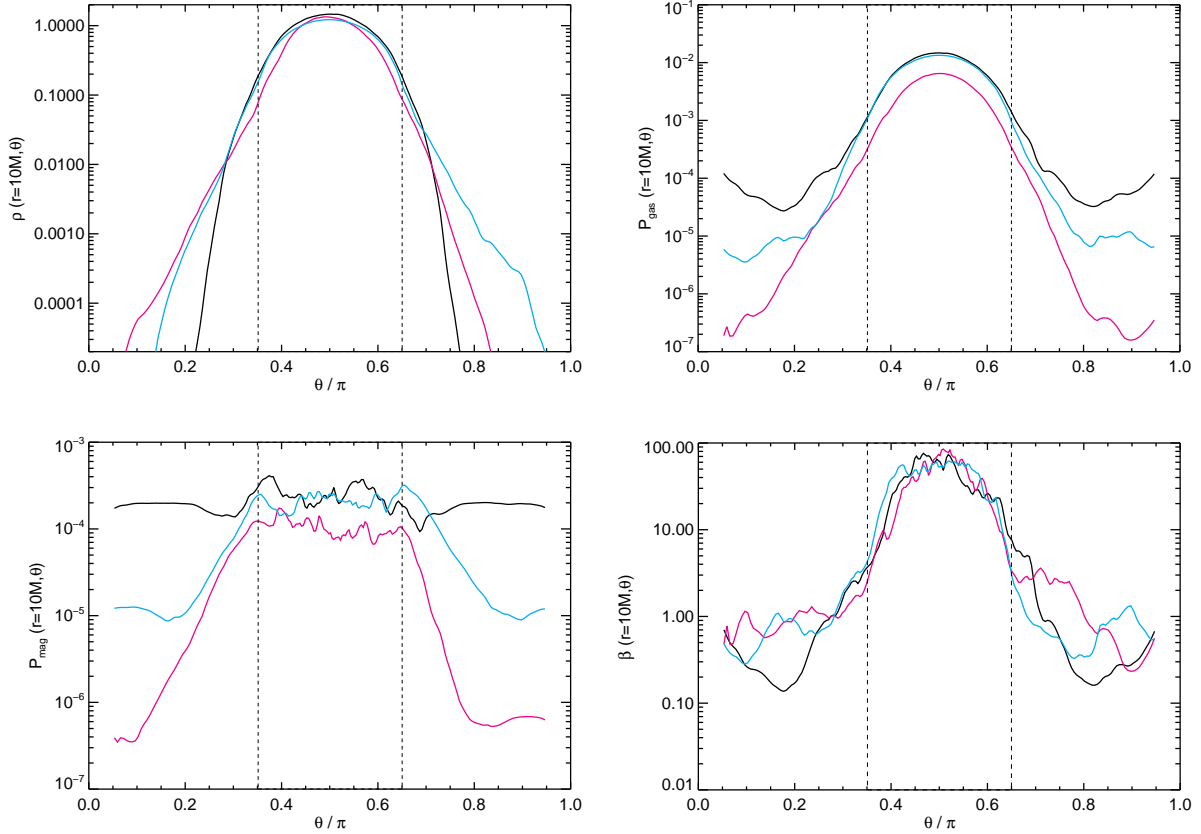
Fig. 6.— Time-averaged angular profiles of density $\langle\rho(\theta; r = 10M)\rangle_A$, gas pressure $\langle P(\theta; r = 10M)\rangle_A$, magnetic pressure $\langle\frac{1}{2}||b||^2(\theta; r = 10M)\rangle_A$ and β parameter $\langle 2P/||b||^2(\theta; r = 10M)\rangle_A$ for simulations KDPg (black lines), QDPa (blue lines) and TDPa (magenta lines). Dotted lines denote the (approximate) boundary of the disk and corona. Note that in the case of TDPa and QDPa, the region of bound matter extends all the way to the axial cutout. KDPg and QDPa are averaged over 8000–$10000M$ and TDPa is averaged over 2–$2.2 \times 10^4 M$.
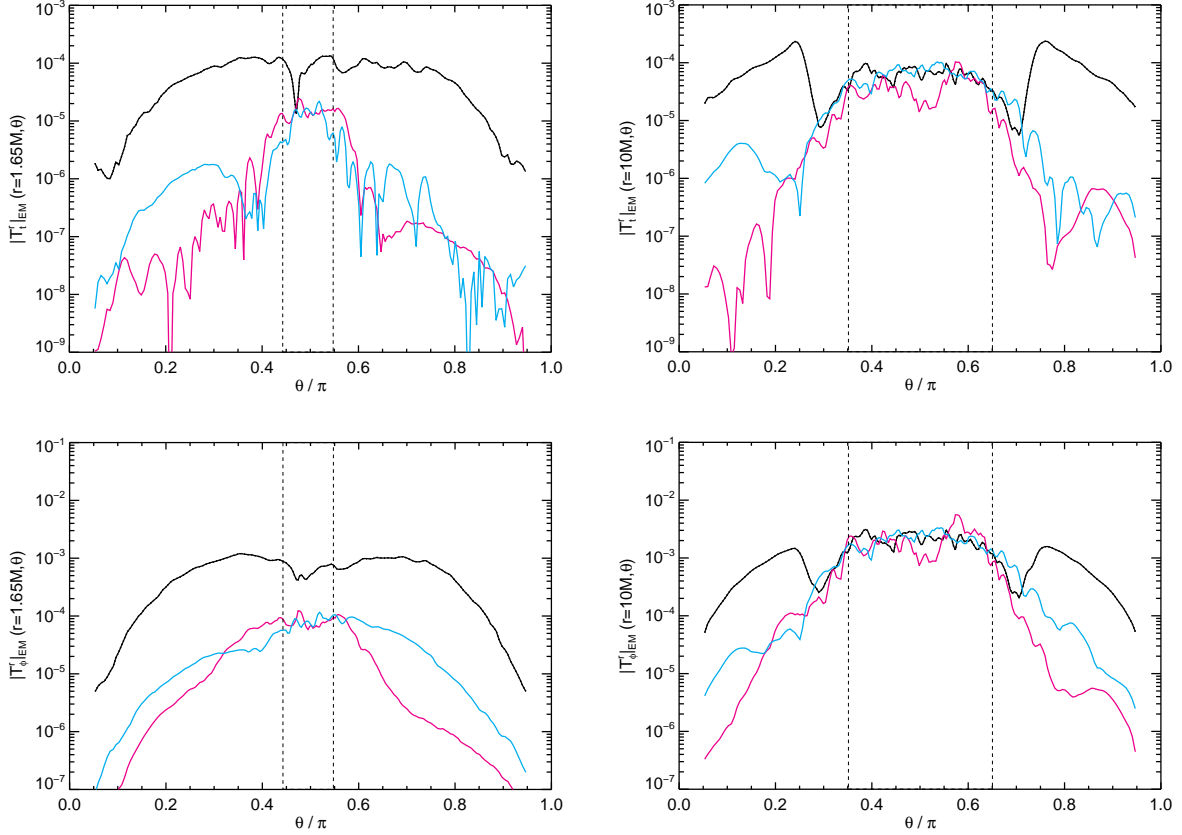
Fig. 7.— Time-averaged angular profiles of $\langle |T_t^r|_{(EM)}(\theta;r)\rangle_A$ (top row) and $\langle |T_\phi^r|_{(EM)}(\theta;r)\rangle_A$ (bottom row) for simulations KDPg (black lines), QDPa (blue lines) and TDPa (purple lines) at $r = 1.65M$ (left column) and $r = 10M$ (right column). Dashed lines denote the (approximate) boundary between the disk body and the corona. KDPg and QDPa are averaged over 8000–$10000M$ and TDPa is averaged over 2–$2.2 \times 10^4 M$.
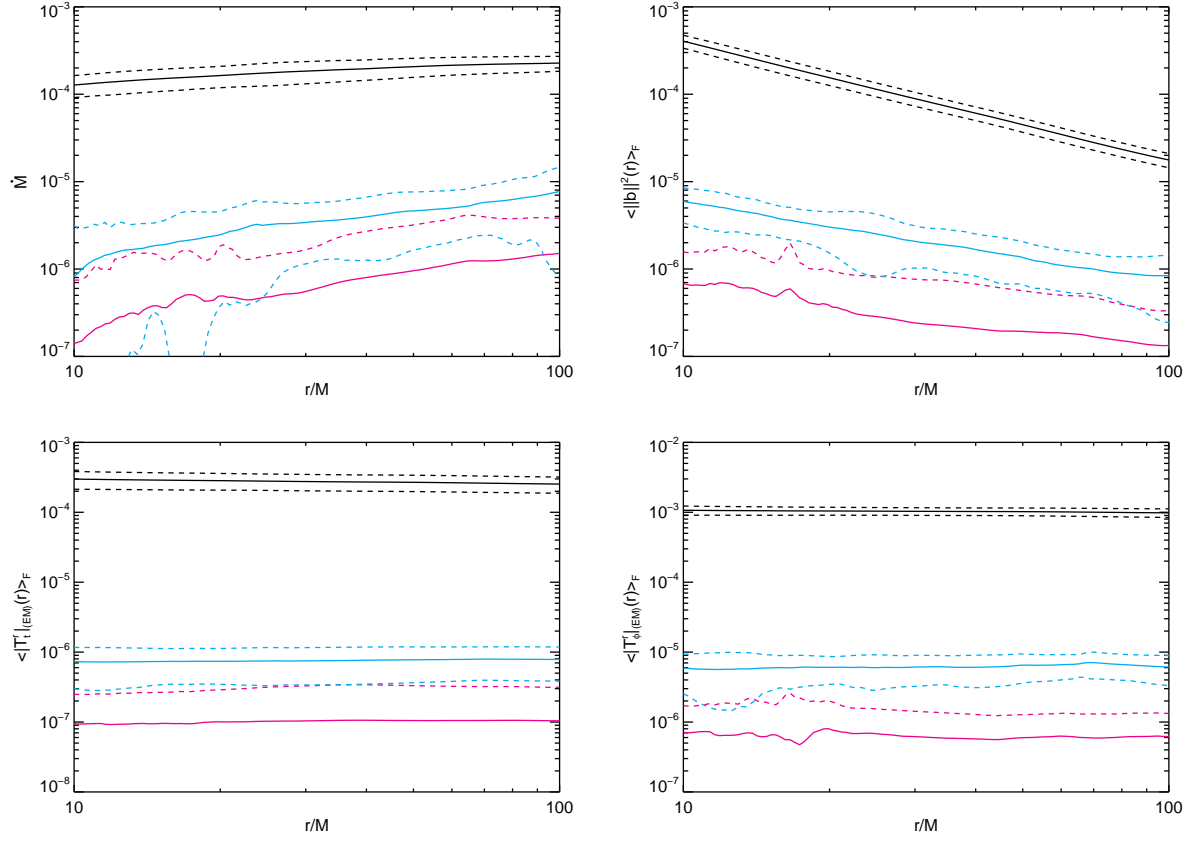
Fig. 8.— Time-average shell integrals of data from unbound outflows as a function of radius for models KDPg (black lines), QDPa (blue lines), and TDPa (magenta lines). Shown are mass outflow rate $\dot{M}$ (top left panel), $\langle||b||^2(r)\rangle_F$ (top right panel); along with the electromagnetic energy flux, $\langle|T^r_t|_{(EM)}(r)\rangle_F$ (bottom left panel) and angular momentum flux $\langle|T^r_\phi|_{(EM)}(r)\rangle_F$ (bottom right panel). KDPg and QDPa are time-averaged over $4000-10000M$ while TDPa is averaged over $12500-18500M$. Dashed lines show ± 1 standard deviation from the average.
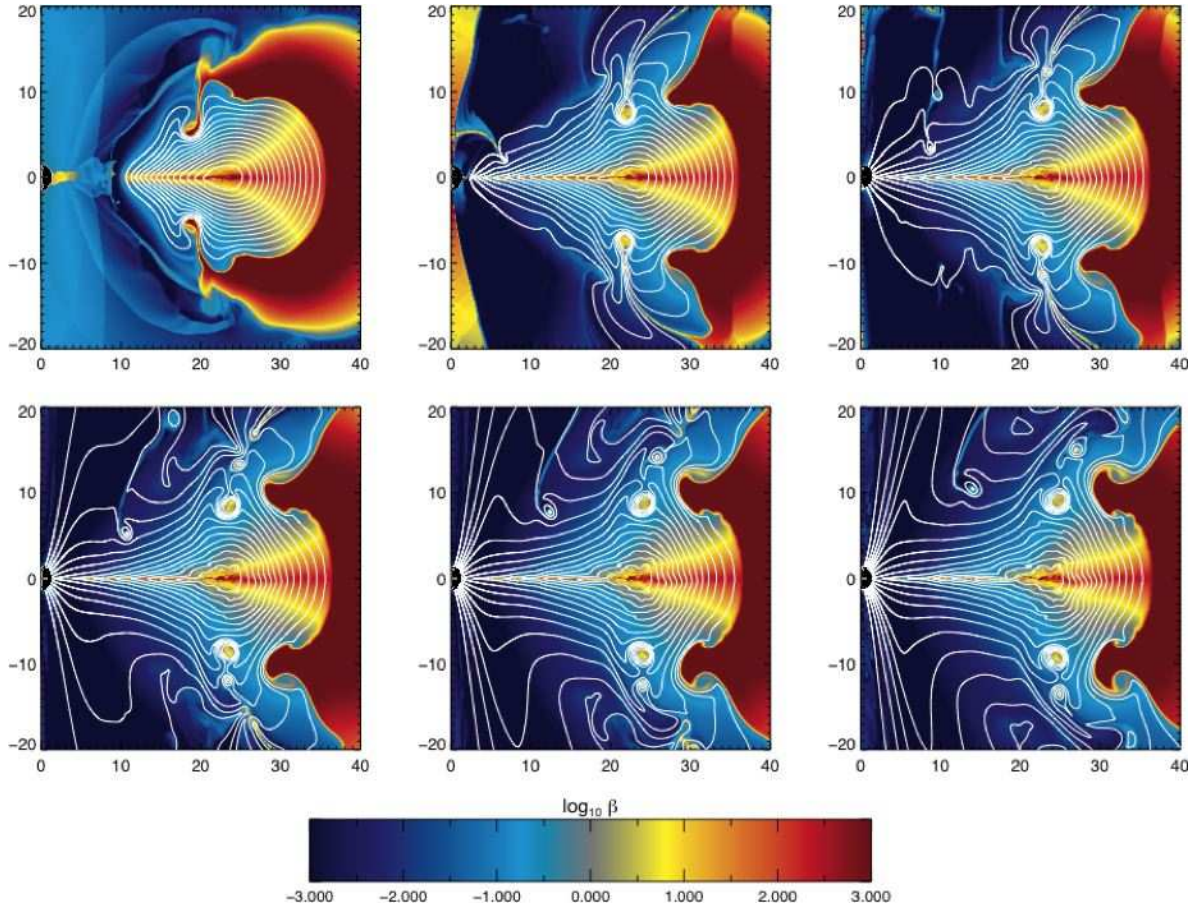
Fig. 9.— Evolution of the magnetic field (white contours) and gas β parameter (filled contours) at $t = 500, 700, 750, 800, 850, 900M$ for the high-resolution, axisymmetric simulation of the dipole field topology. Dark red denotes regions of the simulation that are gas pressure dominated and dark blue denotes regions that are magnetic field dominated.
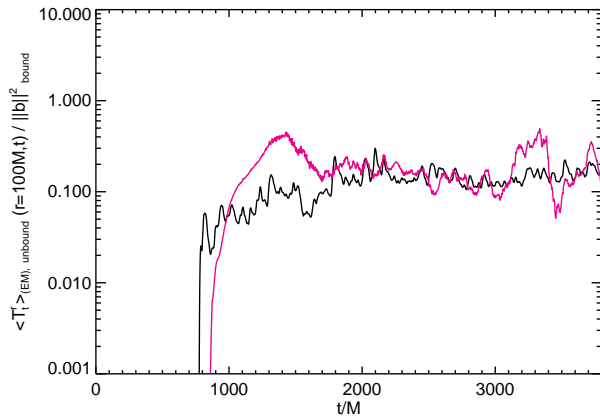
Fig. 10.— Time history of the Poynting flux crossing the $r = 100M$ surface normalized to the total magnetic field strength within the disk for simulation KDPg (black lines) and the high resolution axisymmetric simulation of the dipole (magenta line).
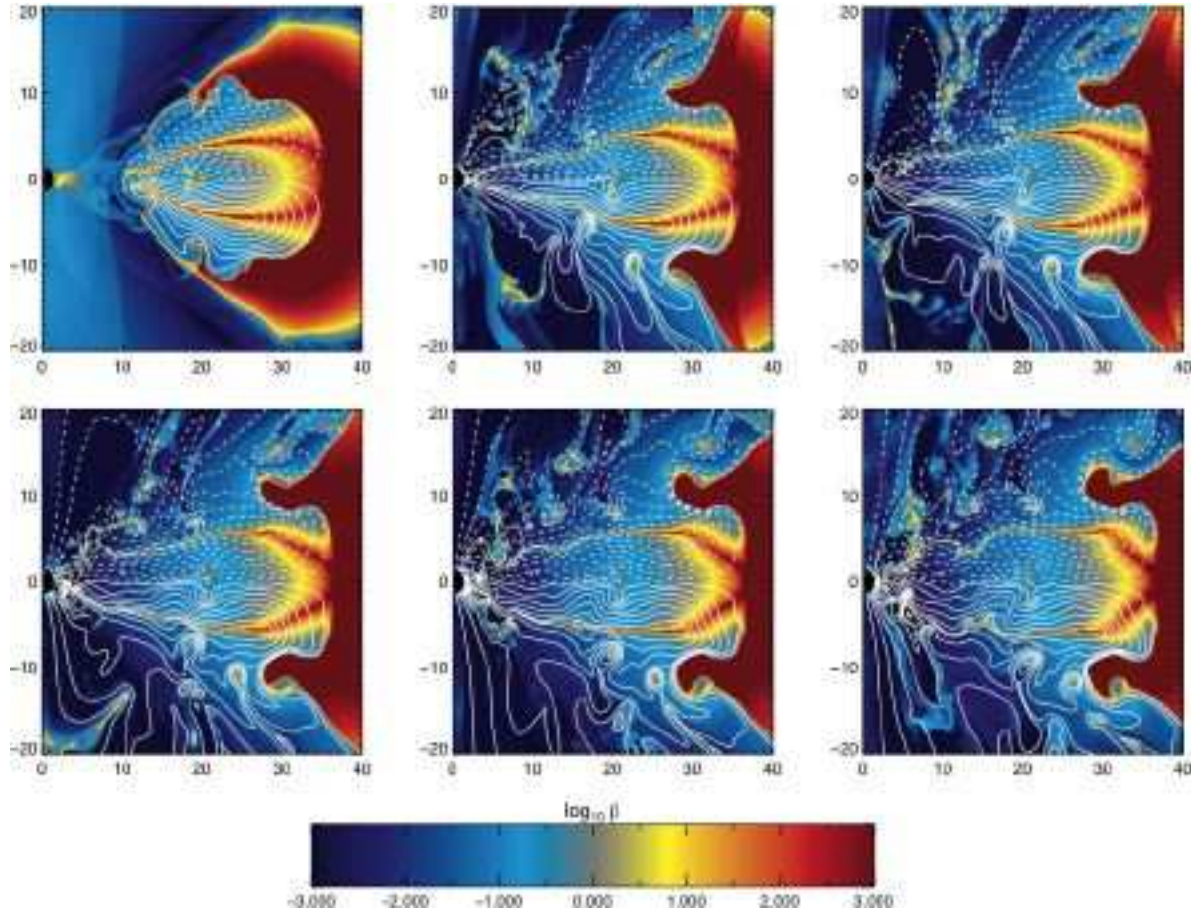
Fig. 11.— Field evolution in the high-resolution, axisymmetric simulation of the quadrupole field topology. Solid white contours denote field lines that have the same parity as the dipole, dashed contours show field lines with the opposite parity. Times shown are the same as in Figure 9.
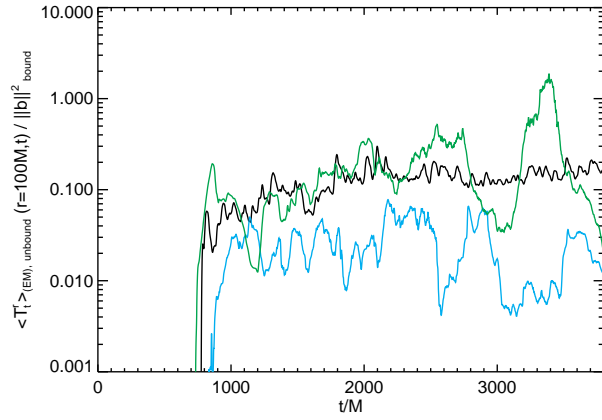
Fig. 12.— Time history of the Poynting flux crossing the $r = 100M$ surface normalized by the total magnetic field strength within the disk. The KDPg dipole simulation is shown in black , the quadrupole simulation in blue, and the multiple loop simulation is green.
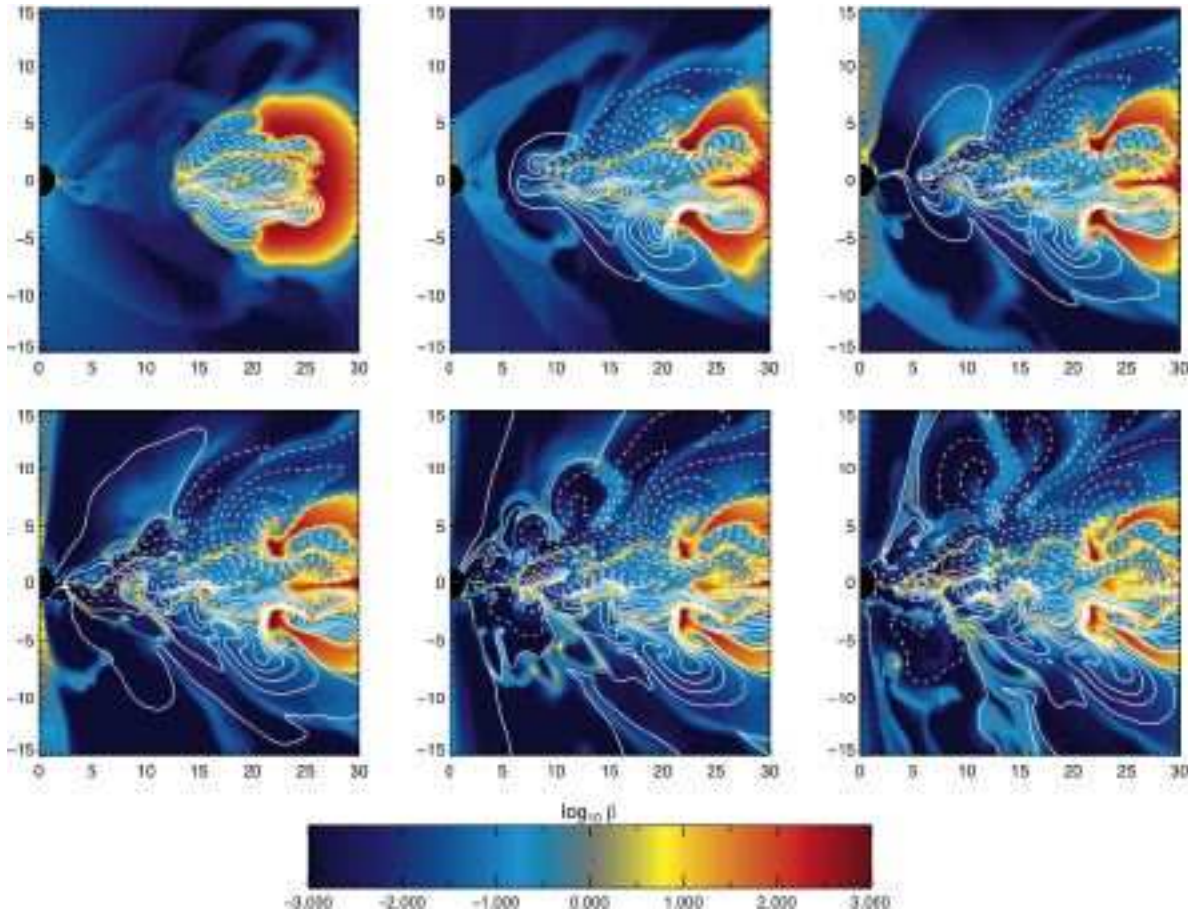
Fig. 13.— As in Figure 11 for the quadrupole field topology overlaid on the narrow $\ell = 4.9$ constant angular momentum torus.
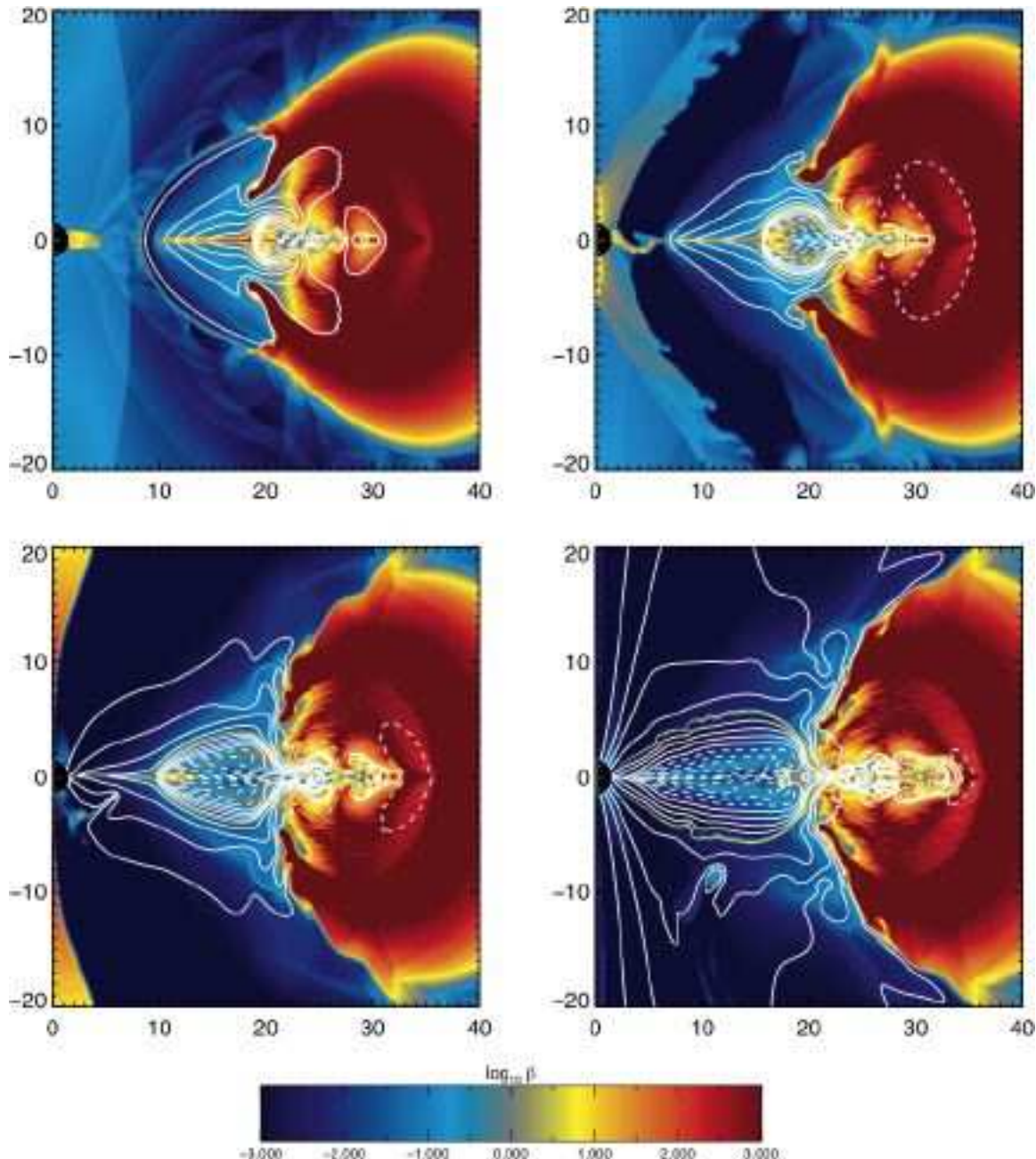
Fig. 14.— Axisymmetric simulation of a series of four narrow dipolar loops at $t = 400, 500, 600, 700M$, showing the initial infall of the innermost loop and subsequent formation of a large-scale dipole field. Solid white contours denote field loops of the same polarity as used in the dipole and quadrupole topologies, dashed white contours denote loops of opposite polarity.
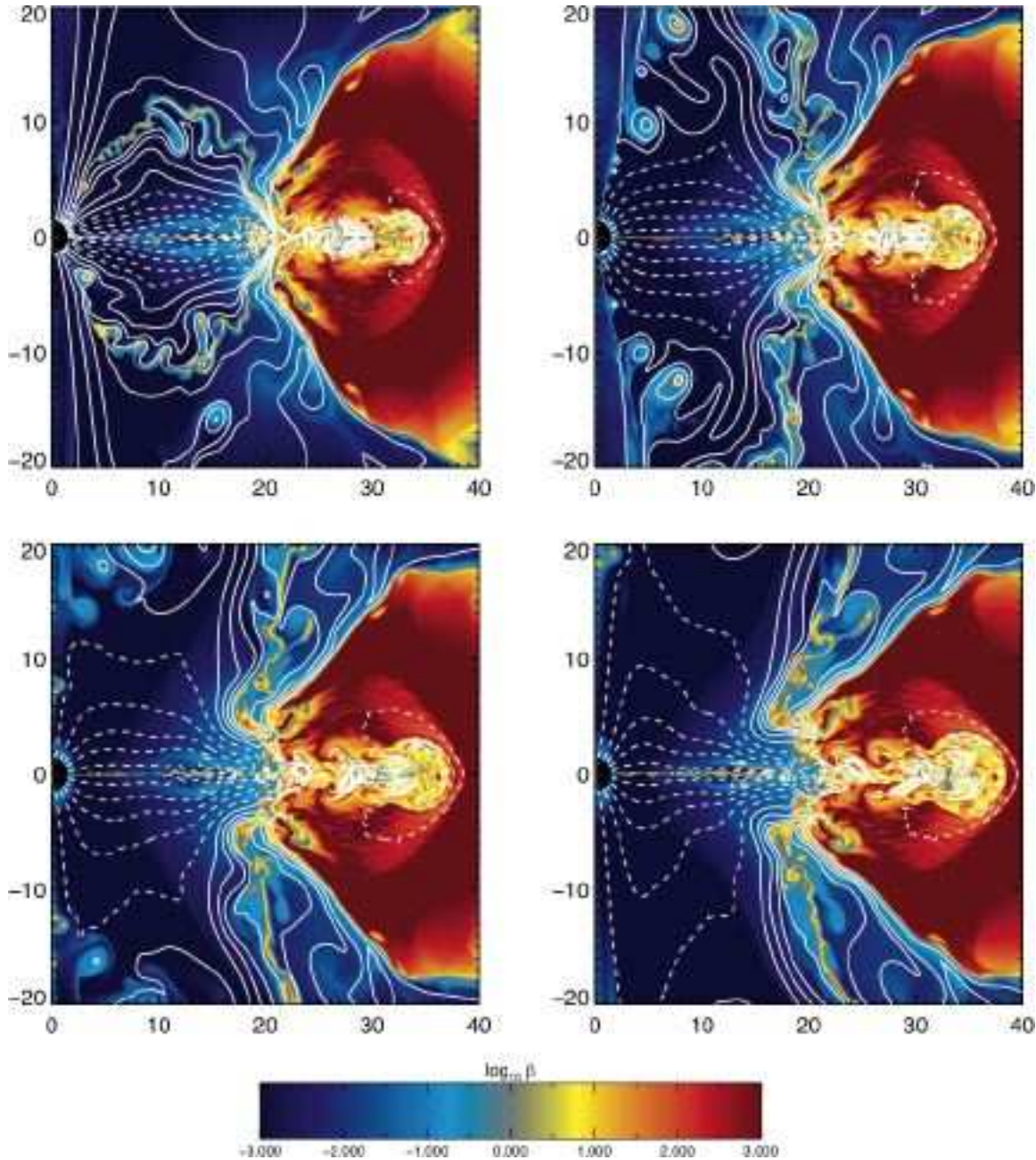
Fig. 15.— As in Figure 14 at $t = 750, 800, 850, 900M$, showing the interaction of the second field loop with the dipole field established by the innermost field loop. The initial dipole field is destroyed but a new large-scale field is subsequently established.
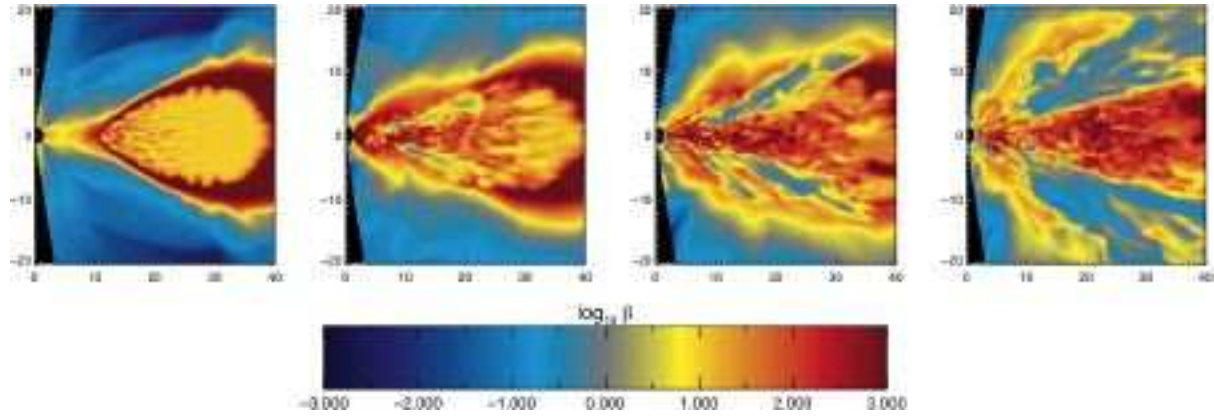
Fig. 16.— Azimuthally averaged gas β parameter in the toroidal field simulation at (from left to right) $t = 2000, 4000, 5600, 7200M$. The equatorial region remains gas pressure dominated throughout the initial evolution, in marked contrast to all of the poloidal topologies.
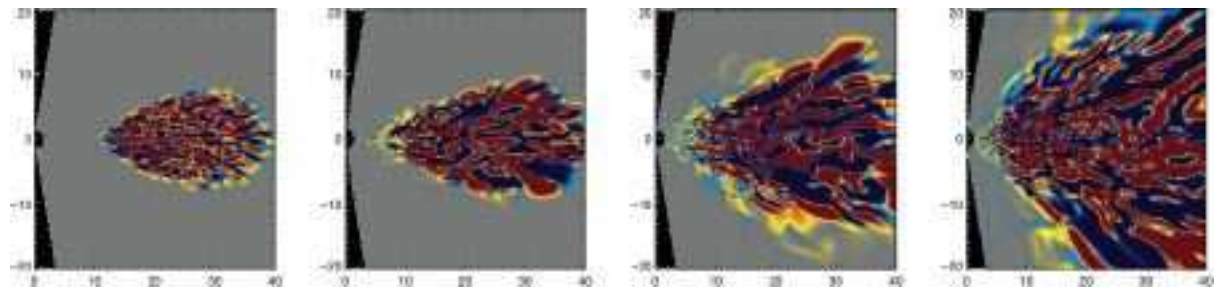

Fig. 17.— Poloidal structure of $\mathcal{B}^r$ for $\phi = 0.25\pi$ in the toroidal field simulation at (from left to right) $t = 2000, 4000, 5600, 7200M$. Red denotes strong, positive field strength, blue strong negative field strength. Grey denotes zero field.